Mineralogy and diagenesis of Mars-analog paleosols from eastern Oregon, USA

Adrian P. Broz* [1,] Joanna Clark[2], Brad Sutter[3], Doug W. Ming[4], Valerie Tu[3], Briony Horgan[5] and Lucas C.R. Silva[6]

[1]Department of Earth Sciences, University of Oregon, Eugene, OR 97405

[2] Geocontrols Systems – Jacobs JETS Contract, NASA Johnson Space Center, Houston, TX, 77058

[3] Jacobs JETS Contract, NASA Johnson Space Center, Houston, TX 77058

[4] NASA Johnson Space Center, Houston, TX, 77058

[5]Department of Earth, Atmospheric and Planetary Science, Purdue University, IN, 47907

[6] Environmental Studies Program, Department of Geography, University of Oregon, Eugene, OR 97405

*Corresponding author, abroz@uoregon.edu

18 **Mineralogy and diagenesis of Mars-analog paleosols from eastern Oregon,**
19 **USA**

20

21 Adrian P. Broz* [1,] Joanna Clark[2], Brad Sutter[3], Doug W. Ming[4], Valerie Tu[3], Briony Horgan[5]
22 and Lucas C.R. Silva[6]

23 [1]Department of Earth Sciences, University of Oregon, Eugene, OR 97405

24 [2] Geocontrols Systems – Jacobs JETS Contract, NASA Johnson Space Center, Houston, TX, 77058

25 [3] Jacobs JETS Contract, NASA Johnson Space Center, Houston, TX 77058

26 [4] NASA Johnson Space Center, Houston, TX, 77058

27 [5]Department of Earth, Atmospheric and Planetary Science, Purdue University, IN, 47907

28 [6] Environmental Studies Program, Department of Geography, University of Oregon, Eugene, OR 97405

29 *Corresponding author, abroz@uoregon.edu

30

31 **Ancient (4.1-3.7-billion-year-old) layered sedimentary rocks on Mars are rich in clay minerals**
32 **which formed from aqueous alteration of the Martian surface. Many of these sedimentary rocks**
33 **appear to be composed of vertical sequences of Fe/Mg clay minerals overlain by Al clay minerals**
34 **that resemble paleosols (ancient, buried soils) from Earth. The types and properties of minerals in**
35 **paleosols can be used to constrain the environmental conditions during formation to better**
36 **understand weathering and diagenesis on Mars. This work examines the mineralogy and diagenetic**
37 **alteration of volcaniclastic paleosols from the Eocene-Oligocene (43-28 Ma) Clarno and John Day**
38 **Formations in eastern Oregon as a Mars-analog site. Here, paleosols rich in Al phyllosilicates and**
39 **amorphous colloids overlie paleosols with Fe/Mg smectites that altogether span a sequence of ~500**
40 **individual profiles across hundreds of meters of vertical stratigraphy. Samples collected from three**
41 **of these paleosol profiles were analyzed with visible/near-infrared (VNIR) spectroscopy, X-ray**
42 **diffraction (XRD), and evolved gas analysis (EGA) configured to operate like the SAM-EGA**
43 **instrument onboard *Curiosity* Mars Rover. Strongly crystalline Al/Fe dioctahedral phyllosilicates**
44 **(montmorillonite and nontronite) were the major phases identified in all samples with all methods.**
45 **Minor phases included the zeolite mineral clinoptilolite, as well as andesine, cristobalite, opal-CT**
46 **and gypsum. Evolved H_2O was detected in all samples and was consistent with adsorbed water and**
47 **the dehydroxylation of a dioctahedral phyllosilicate, and differences in H_2O evolutions between**
48 **montmorillonite and nontronite were readily observable. Detections of hematite and zeolites**
49 **suggested paleosols were affected by burial reddening and zeolitization, but absence of illite and**
50 **chlorite suggest that potash metasomatism and other, more severe diagenetic alterations had not**
51 **occurred. The high clay mineral content of the observed paleosols (up to 95 wt. %) may have**
52 **minimized diagenetic alteration over geological time scales. Martian paleosols rich in Al and Fe**
53 **smectites may have also resisted severe diagenetic alteration, which is favorable for future *in-situ***
54 **examination. Results from this work can help distinguish paleosols and weathering profiles from**
55 **other types of sedimentary rocks in the geological record of Mars.**

56

57

1. Introduction

Today the surface of Mars is frigid, wind-deflated and barren, but there is extensive geological evidence for transient warm and wet habitable surface conditions in the Noachian (4.1–3.7 Ga) period of early Mars [1–4]. Orbital sensing of the Martian surface has revealed clay mineral deposits in thousands of locations, wherever Noachian-age terrains are not obscured by dust, sand, or overlying strata [5–8]. These ancient deposits are rich in smectite clay minerals and other hydrated phases, suggesting formation in subsurface and surface environments from the weathering of mafic rocks and sediments with liquid water.

While some phyllosilicates on Mars are associated with lacustrine deposition in surface environments (e.g., [9]) many phyllosilicate detections occur in regionally widespread deposits, inconsistent with deposition in basin settings. Two hypotheses to explain the formation, occurrence and distribution of these regionally widespread phyllosilicates on Mars are: 1) subsurface hydrothermal activity, diagenesis and/or authigenesis [10–14] and, 2) surface pedogenic alteration (e.g., subaerial chemical weathering) [2,6,14,15]. In some locations, trioctahedral smectites exhibiting lateral variations in Al and Fe/Mg smectites intermixed with chlorite, serpentinite, talc and zeolite are consistent with formation in hydrothermal subsurface environments, diagenesis, and/ or authigenesis during sediment emplacement [13,16,17]. However, dioctahedral smectites often outcrop as extensive vertical profiles of Fe/Mg smectites overlain by Al smectites, suggesting subaerial formation in surface environments, consistent with pedogenesis (soil formation) or large-scale leaching of sediments [14].

Paleosols are ancient, buried soils that are lithified into sedimentary rocks. On Earth, paleosols are a geological record of the atmospheric composition, climate, topography and organisms present before soil burial [18]. Paleosols are created by removal from their soil-forming factors, sometimes because of change in those factors, but most often by rapid burial. The deposition of volcanic ash, flood basalts, sedimentation from flooding, landslides, and tsunamites all rapidly bury surface environments. Sequences of paleosols form when soils are periodically buried, for example by repeated volcanic eruptions which emplace tephra or lava onto soil surfaces, followed by successive pedogenic weathering of emplaced tephra or lava, and then subsequent burial by another eruption. Flooding by rivers also buries paleosols within alluvial sequences, and dune migration buries paleosols within eolian sequences. On Earth, sequences of paleosols formed by periodic burial can record weathering, paleoclimate and diagenetic alteration over 10^7 year timescales [19,20].

Paleosols can be useful tools for interpreting ancient climates of Earth and Mars [21–23]. The types and properties of minerals in Mars-analog paleosols can be used to help understand the nature of weathering and diagenesis on Mars [24,25] but they remain relatively understudied as Mars-analog sites. The objective of this study was to examine the mineralogy and diagenetic alterations of Mars-analog paleosols from eastern Oregon, USA using analytical techniques similar to those onboard current and future missions to Mars.

1.1 Paleosols at John Day Fossil Beds National Monument

The John Day Fossil Beds National Monument in eastern Oregon, USA, is an established Mars-analog site known for similarities in mineralogy and stratigraphy to clay-bearing sedimentary rocks on Mars [20,26,27]. Here, Eocene and Oligocene (42-28 Ma) sedimentary rocks are a well-preserved sequence of andesitic to rhyodacitic paleosols [15,28–30]. The ~400-meter-thick sequence is host to over 500 individual clay mineral-rich (30-95 wt. %) paleosols spanning 15 Myr through the climatic cooling of the Eocene-Oligocene boundary (Figure 1). A record of dramatic climate change is preserved in the mineralogy of paleosols from the Eocene/Oligocene-age Clarno and John Day Formations, transitioning from high kaolinite and oxide abundances at the bottom (warm and wet Eocene), to high smectite abundances (drying out late Eocene), and then poorly crystalline phases at the stratigraphic top of the section (cool and dry Oligocene) [28,29].

Figure caption (right side, associated with photos):

Turtle Cove member, John Day Formation
MAP 400-600 mm
Amorphous Al / Si, celadonite, zeolites

middle Big Basin member (this study)
MAP 600-1200 mm, MAT 16-18° C
Al/Fe smectite, hematite, goethite

Clarno Formation "brown grotto"
MAP 900-2000 mm, MAT 23-25° C
Oxides, kaolinite, Fe/Mg smectite

Stratigraphic column labels:

Picture Gorge ignimbrite (28.7 Ma)
upper white tuff (28.8 Ma)
lower Turtle Cove Member
sanidine tuff (29.8 Ma)
upper Big Basin Member
Overlook tuff (32.7 Ma)
middle Big Basin Member
biotite tuff (33.0 Ma)
andesite breccia
andesite breccia of Sand mtn. (37 Ma)
lower Big Basin Member
John Day Member A (39.7 Ma) — **JOHN DAY FM**
red laterites of "brown grotto" — **CLARNO FM**
red claystones of Sand Mtn.
andesite of Bridge Creek canyon
red and purple claystones of Meyers Canyon
lower Clarno andesite flows

Legend: claystone paleosols | root traces | andesite | tuff layer

Figure 1. A sequence of Eocene through Oligocene (43-28 Ma) volcaniclastic paleosols in the Clarno and John Day Formations, John Day Fossil Beds National Monument (redrawn from [28]. Mean annual precipitation (MAP) and mean annual temperature (MAT) estimates are from Retallack et al (2000) [31].

Stratigraphically lowest in the section are deeply weathered red and purple lateritic paleosols (Oxisols and Ultisols in US Taxonomy [32]) within the uppermost Clarno and lowermost John Day Formations in the Painted Hills (~42 Ma). These paleosols formed under a warm and wet climate of an estimated 900-2000 mm mean annual precipitation (MAP) and mean annual temperature (MAT) of 23-25° C [29] (Figure 2). This unit of the section generally resembles the basal Fe/Mg clay unit at Mawrth Vallis [20]. The Clarno paleosols have accumulations of oxides, kaolinite and Fe/Mg smectites and are

115   erosionally truncated and abruptly overlain by less deeply weathered Al/Fe smectite-rich paleosols
116   (Inceptisols and Alfisols) of the middle Big Basin Member of the John Day Formation (~33 Ma, samples
117   from this location examined in this study). This truncation surface is correlated with the international
118   Eocene-Oligocene boundary [29]. Big Basin member soils appear to have formed under a markedly cooler
119   (MAT 16-18° C) and drier (MAP 600-1200 mm) climate relative to the early Eocene [31]. Stratigraphically
120   above, in the Turtle Cove paleosols, another erosional truncation marks the base of the late Oligocene
121   (~28 Ma) lower Turtle Cove Member of the John Day Formation which has minimally weathered
122   calcareous paleosols (Aridisols and Andisols) containing abundant celadonite, calcite and amorphous
123   colloids (imogolite, ferrihydrite and allophane) which indicate an even drier (MAP 400-600 mm) climate
124   during the late Oligocene [33].

126
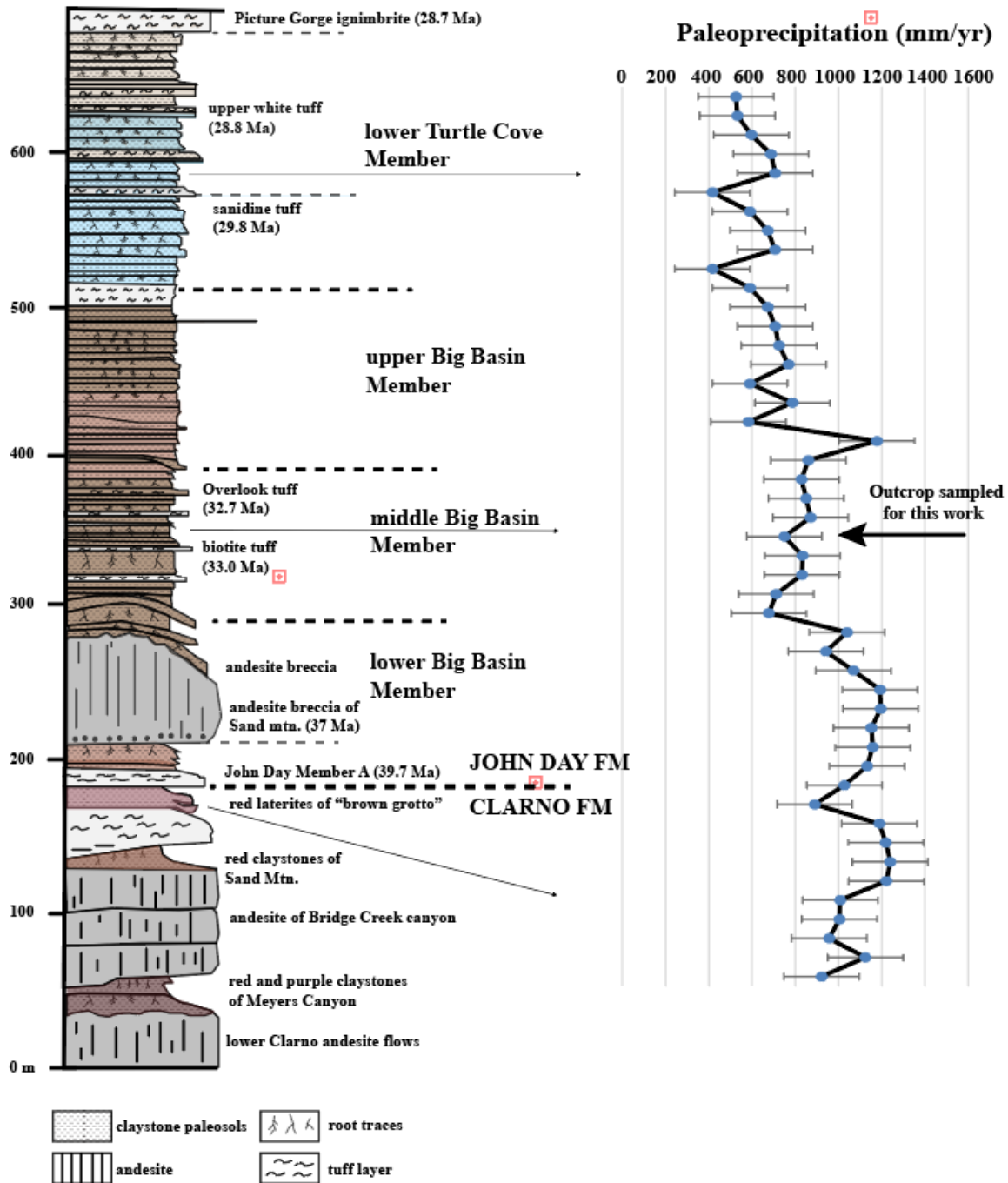
Figure 2. Declining precipitation through the Eocene/Oligocene boundary inferred from the mineralogy of paleosols from the Clarno and John Day Formations (after Bestland et al. (1997) and Sheldon et al (2002). The stratigraphic level of paleosols analyzed in this work is indicated (black arrow). Paleoprecipitation estimates are from Sheldon et al (2002) are from an equation relating molecular weathering ratios (Bases/alumina [CaO + MgO + Na$_2$O + K$_2$O / Al$_2$O$_3$] to mean annual precipitation from a database of modern U.S soils (r=0.79, standard error = 179 mm) [31].

133   The Turtle Cove Member (late Oligocene) is composed of light brown and green colored Andisol
134   (volcanic soils) and Aridisol (desert soils) paleosols that overlie the upper Big Basin member of the John
135   Day Formation. The Turtle Cove Member has increased amounts of amorphous phases and calcite as well
136   as the blue to green-colored clay mineral celadonite. Celadonite in the Turtle Cove paleosols is thought to
137   form from the recrystallization of poorly crystalline smectite and/ or amorphous phases [29]. Although
138   spectral signatures of celadonite and/or glauconite have been noted in the Mawrth Vallis region [34], it is
139   currently unclear if celadonite is a component of putative Martian paleosols. In any case, the Turtle Cove
140   paleosols have a dramatic reduction in smectite abundance and near absence of kaolin-group clays
141   relative to the Clarno Formation paleosols at the base of the section [15,29]. Similarly, the accumulation of
142   amorphous / nanocrystalline phases is observed at the stratigraphic top of the Noachian-age section at
143   Mawrth Vallis [35] which is consistent with a drier, colder climate that was not sufficient to weather
144   volcanic ash into more crystalline phases.
145   Stratigraphically above the Turtle Cove Member paleosols, approximately 300 vertical meters of
146   flood basalts from the Columbia River Group cap the entire sequence. Based on these mineralogical
147   transitions, the Eocene-age paleosols at the base of the section have accumulations of kaolinite and oxides
148   that reflect a subtropical and humid climate, late Eocene/ early Oligocene paleosols in the middle of the
149   section have Al/Fe smectites associated with a more arid climate, and paleosols with accumulations of
150   nanophase aluminosilicates and amorphous phases higher in the stratigraphy indicate stepwise and
151   cooling and drying during the late Oligocene [29]. Sequences of paleosols within the John Day Formation
152   are similar in mineralogy and stratigraphy to dioctahedral clay mineral sequences at Mawrth Vallis [15,26]
153   and record a stepwise cooling and drying similar to proposed climates of early Mars.
154
155   **1.2 Comparisons to putative Martian paleosols**
156   Remote sensing of the Martian surface has revealed Noachian-age (4.1-3.7 Ga) layered sedimentary
157   rocks rich in dioctahedral clay minerals that appear to be distributed globally across the surface of Mars
158   [6,7,14]. These rocks are generally characterized by strong spectral signatures of Al clays overlying Fe/Mg
159   clays over hundreds of vertical meters of stratigraphy. One hypothesis for their formation is from
160   pedogenic weathering of mafic sediments such as volcanic ash during intermittent warm periods early in
161   Mars' history [6,14,24,36]. These altered sediments are detected mantling topographic highs including the
162   summits and flanks of volcanoes, consistent with formation in surface environments via pedogenic
163   weathering [4]. Many of the clearest examples of putative Martian paleosols are observed in crater rims [15,26].
164   The rim of Muara Crater at Mawrth Vallis is host to a 150 – 200 m thick Fe/Mg smectite unit (topped
165   by sulfate deposits in some areas) overlain by a 50 m thick Al-phyllosilicate or opal unit which transitions
166   upward into poorly crystalline aluminosilicates or nanophase materials [37,38]. The entire section is then
167   capped by an igneous deposit which appears to be composed of lava and/or basaltic sand [14], similar to the
168   stratigraphy of the John Day Formation paleosols which are capped by approximately 300 meters of flood
169   basalts. The layering of dioctahedral Al clay minerals and Fe/Mg clay minerals over hundreds of vertical
170   meters suggests a subaerial formation environment for the clay minerals [14,24], and therefore congruent
171   pedogenic alteration of basaltic parent material under warm and wet conditions is one hypothesis to
172   explain the exceptional thickness of the Mawrth Vallis sequence [6,15,39,40].
173   The compositional stratigraphy at Mawrth Vallis has been proposed to be either a paleosol sequence
174   [15] or a deep weathering profile (e.g., saprolite mantle) [24]. Terrestrial paleosol sequences are stacks of
175   individual, meter-scale weathering profiles that form from repeated pedogenic alteration followed by
176   burial. With repeated pedogenic alteration and burial by tephra or lava over 10^6-10^7 yr scales,
177   volcaniclastic sequences of individual paleosol profiles can reach hundreds to thousands of meters in
178   vertical thickness [41,42]. Rapid burial of each paleosol surface via emplacement of tephra or lava can also
179   create favorable conditions for the preservation of biosignatures. In terrestrial settings, each individual
180   profile within the sequence typically accumulates and preserves organic carbon in the near-surface layers,
181   just below the uppermost burial layer [43], which often presents at field scale as a nonconformity [18]
182   By contrast, deep weathering profiles are the products of intense, long-term chemical weathering
183   across tectonically stable landscapes and instead are characterized by a single, massive, and uninterrupted

184 weathering profile. They are most common at terrestrial intertropical latitudes between 35° N and 35° S
185 [44]. The vertical extent of deep weathering profiles, which includes weathered residuum and sediments
186 overlying basement rocks, varies from a few meters to over 150 meters, dependent on climate, tectonic
187 activity, age of the land surface and the properties of the bedrock [44,45]. The generally flat-lying
188 topographic relief of deep weathering profiles allows for leaching of weathering products, usually when
189 the downward progression of the weathering front exceeds the erosion rate [45]. The weathering front
190 typically obliterates any primary sedimentary structures such as relict bedding of the basal unweathered
191 layers in each profile (C and R horizons in US Soil Taxonomy). The organic preservation potential of
192 terrestrial deep weathering profiles (e.g., laterites) is generally considered to be poor, largely in part due
193 to leaching and/or oxidation of endogenous organic molecules derived from surface biomass [46]. However,
194 Noachian (4.1-3.7 Ga) surface weathering may have proceeded under an anoxic atmosphere and was
195 possibly similar in nature to Archean (4.1-2.6 Ga) anoxic pedogenic weathering on Earth. Reducing
196 conditions during ancient pedogenic weathering creates favorable taphonomic conditions for the
197 preservation of biosignatures over geological time scales, including carbonaceous microfossils [47] and
198 organic carbon associated with mineral surfaces [48,49]. Therefore, distinguishing between paleosol
199 sequences and deep weathering profiles has major implications for paleoclimate interpretations and
200 biosignature preservation throughout the Mawrth Vallis region [14].
201   The thickness of the Mawrth Vallis compositional stratigraphy (~150 -200 m) exceeds the thickness
202 of terrestrial deep weathering profiles (typically less than 100 m). The stratigraphy could have resulted
203 from sediment deposition and then extensive vertical leaching by liquid water during post-depositional
204 diagenesis, but such deep leaching profiles on Earth rarely exceed 150 m in thickness [15]. The exposed
205 stratigraphy at Mawrth Vallis also appears to have lateral and vertical diversity beyond the overall Fe/Mg
206 smectite – Al-Si phase stratigraphy [15]. Lateral and vertical diversity of clay minerals is not found in deep
207 weathering profiles but is common in paleosols, which have diversity in composition and color at ~1-
208 meter scales. However, the 18 meter/pixel resolution of CRISM [5] may limit interpretations of the
209 mineralogical diversity of these deposits on Mars because the fine-scale features of paleosols may be
210 obscured at these resolutions. There also appears to be relict bedding of dark-toned sands throughout the
211 deposit, which suggests the coarse-sized fraction of the parent material may be preserved in certain layers
212 as less-weathered bottom layers (C and R horizons) of paleosols. This relict bedding would presumably
213 be destroyed if the entire deposit was a deep weathering profile [15]. Dioctahedral phyllosilicate layers at
214 Mawrth Vallis may be a paleosol sequence that formed under a semi-arid climate, overlain by a thinner
215 leaching profile and capped by a relatively unaltered igneous deposit [20,50]. This stratigraphy is consistent
216 with climate hypotheses for early Mars, including a Noachian hyperarid frigid paleoclimate alternating
217 with warmer and wetter conditions [14,25]. A similar pedogenic-like stratigraphy of dioctahedral Al clays
218 overlying Fe/Mg clays has been detected in hundreds of locations across the surface of Mars which
219 suggests widespread surface weathering was not limited to the Mawrth Vallis region [6,7]. Since many of
220 the layered clay mineral sequences on Mars resemble terrestrial paleosols [51], a detailed mineralogical
221 analysis of paleosols from Earth can help with identification and interpretation of these deposits.
222   It is important to note that the results from this study alone cannot determine if the Mawrth Vallis
223 stratigraphy is a paleosol sequence or a deep weathering profile. Rather, this study seeks to determine if
224 pedogenic and diagenetic features in ancient terrestrial samples can be identified with a multi-instrument
225 suite relevant to current and future missions on Mars. This determination is a critical first step to constrain
226 the formation mechanisms of possible pedogenic deposits on Mars.
227
228 **1.3 Terrestrial analogs as a window into surface weathering on Mars**

229   In this study, we examined early Oligocene (33 Ma) paleosol profiles from the Mars-analog paleosol
230 sequence in eastern Oregon (Figure 2). Orbital and *in-situ* visible-near infrared (VNIR) spectroscopic
231 techniques are used by current and future missions to Mars and are a useful tool for identifying minerals
232 and diagenetic features across the global Martian surface [5,52,53]. Here, *in-situ* visible-near infrared
233 spectroscopy was performed to identify clay minerals, zeolites and oxides in bulk paleosol samples. The

234 *Curiosity* Mars rover employs *in-situ* X-ray diffraction (XRD) for identification and quantification of
235 crystalline minerals in rocks, sediments and soils on Mars [54,55]. Qualitative X-ray diffraction was used in
236 this study to identify crystalline minerals in bulk paleosol samples from the three consecutive paleosol
237 profiles. Lastly, samples were analyzed with an instrument calibrated to use analytical conditions similar
238 to the Sample Analysis at Mars evolved gas analysis (SAM-EGA) instrument onboard the *Curiosity* rover
239 [56]. The purpose of this analysis was to constrain the mineralogy of hydrated phases in samples,
240 specifically by examining evolutions of H_2O and SO_2 from bulk paleosol samples during heating. Since
241 thermal techniques such as evolved gas analysis will fly onboard future missions to Mars (e.g. ExoMars
242 2022 Rosalind Franklin rover [57]), a detailed characterization of terrestrial paleosol mineralogy via evolved
243 gas analysis can help constrain the formation mechanism(s) of dioctahedral clay-bearing sedimentary
244 rocks on Mars.

2. Methods

2.1 Sample collection

247 The paleosols examined in this study were collected from the Middle Big Basin Member of the
248 John Day Formation (Figure 2) near the Painted Hills Unit of the John Day Fossil Beds National
249 Monument in eastern Oregon, USA. For this work, we reoccupied paleosol profiles first described and
250 sampled by Retallack et al. (2000) [29]. New samples from three individual paleosols in vertical succession
251 were collected approximately 7 km SW of the entrance to the Painted Hills unit of the John Day
252 Formation (44.631105, -120.213107), in the Middle Big Basin Member of the John Day Formation,
253 approximately 6 m above the local Eocene-Oligocene boundary (Figure 2). Samples were chosen from
254 this site because it contained a sequence of three successive paleosols at a general topographic position
255 (e.g., badland toeslope) that may be accessible for *in-situ* analysis on Mars by future landed missions
256 including rovers and /or astronauts. Furthermore, previous $^{40}Ar/^{39}Ar$ dating of volcanic tuffs above and
257 below the sampling location allowed for a constrained age of 33.0 +/- 0.10 to 32.7 +/- 0.03 Ma (Biotite
258 Tuff and Overlook Tuff, respectively) [28].

259 Samples were collected by first trenching to ~30 cm into the outcrop to remove the modern
260 weathering zone and to expose the underlying claystone paleosols. This was followed by sampling with a
261 rock hammer down a vertical transect (parallel with the hillslope) at approximately 10 cm intervals,
262 similar to sampling the horizons of a modern soil profile. Large, ~0.2 kg lithified blocks were removed
263 from the brick-like paleosol surface for mineralogical analyses. The morphology, Munsell color and
264 qualitative calcareousness of samples were also described during collection **(Figure 3)**.

265 The same paleosol profiles were previously analyzed for bulk geochemistry by Retallack et al.
266 (2000) and those values were used to calculate chemical index of alteration and molar weathering ratios to
267 augment our mineralogical assessment of the same samples (see Results).The three paleosols sampled
268 were a red Alfisol ("Luca" pedotype from Retallack et al. (2000) [29], a tan Entisol ("Kskus" pedotype), and
269 a brown Inceptisol ("Ticam" pedotype). In modern soil taxonomy, Alfisols are moderately weathered
270 soils typically forming in semi-arid to humid climates under broadleaf temperate forests and are
271 characterized by a clay-enriched subsurface horizon (layer) as well as accumulations of Al and Fe,
272 lending the "Alf" of Alfisol. Entisols are minimally developed soils which are characterized by a lack of
273 pedogenic horizon development and are generally minimally altered from their parent material.
274 Inceptisols are "new soils" and typically have only weak development of horizons produced by top-down
275 pedogenic weathering [32].

276
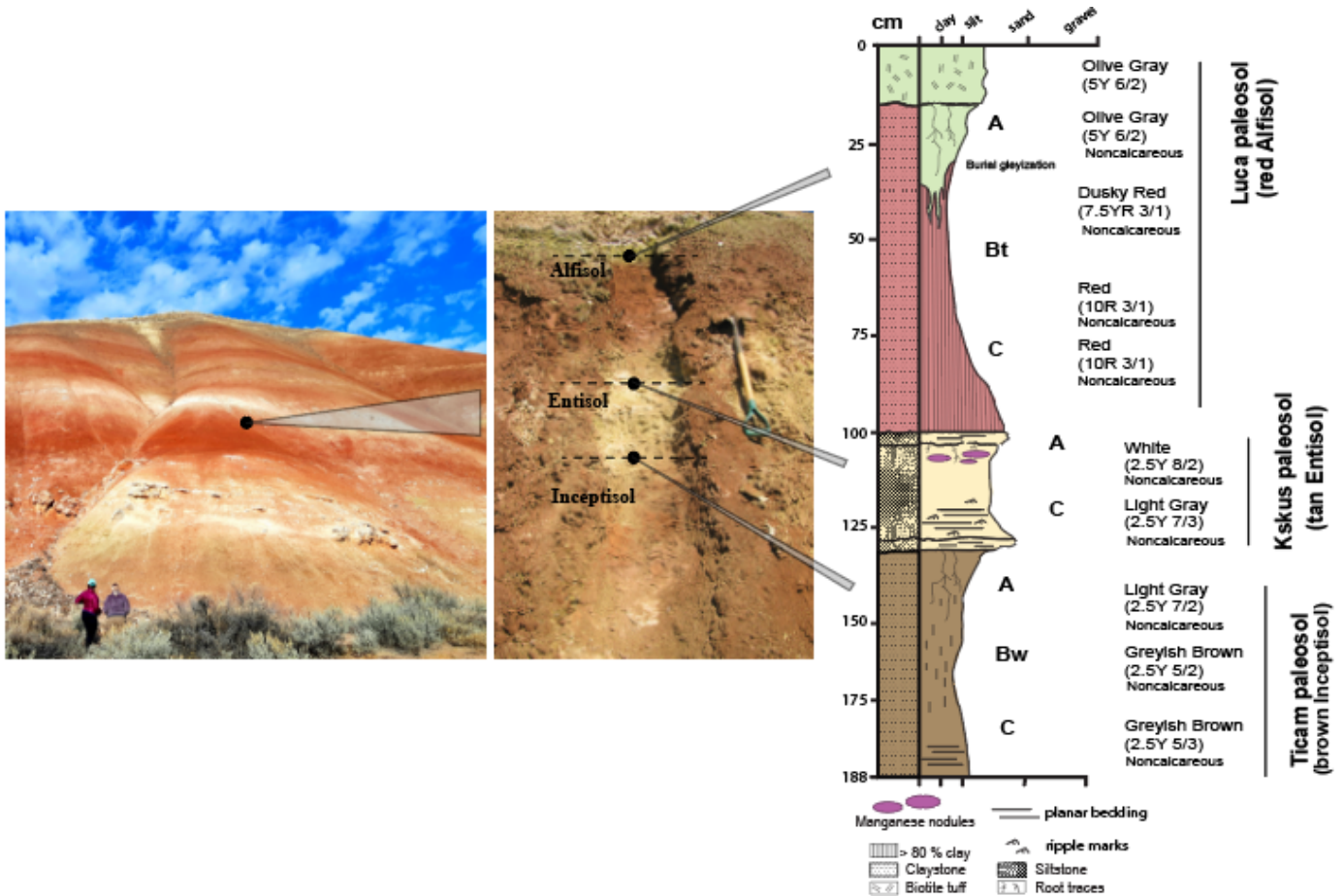
Figure 3. Morphology of three successive paleosols examined in this work. Paleosols are from the early Oligocene (33 Ma) middle Big Basin Member of the John Day Formation in eastern Oregon, USA showing lithology, grain size, horizon designations, and Munsell color. The upper paleosol (red with drab green top) is a moderately weathered Alfisol (Hapludalf in US Taxonomy [32]) with a clay-enriched subsurface (Bt) horizon; stratigraphically below is a minimally weathered and weakly developed Entisol with minimal pedogenic horizon development and persistent relict bedding in the subsurface (C) horizon (Fluvent in US Taxonomy, tan color); the lowest soil (brown color) is an Inceptisol with slight enrichment of clay into a weakly-developed subsurface (Bw) horizon (Andic Eutrochrept in US Taxonomy).

2.4 Visible-near infrared spectroscopy

Reflectance spectra of paleosols was measured on hand samples collected from the outcrop using a portable ASD QualitySpec Trek spectrometer (Analytik, Cambridge, UK). Reflectance features from 0.35 – 2.5 μm of samples were measured indoors at ambient (25 °C) temperature at the Condon Paleontology Center at the John Day Fossil Beds National Monument, and samples were not ground or sieved before analysis. Dioctahedral clay mineralogy was inferred from cation-OH combination bands in the 2.2 – 2.5 um region [58]. Band centers between 2.12 – 2.21 microns indicated the presence of Al-smectite. Fe/Mg clays and carbonates were identified from absorption bands between 2.27 and 2.36 microns while oxides were identified from bands between 0.75 – 1.03 microns. Absorption bands from zeolites are noted across the 2.1-2.5-micron range which overlap with Si-OH and/or metal-OH absorption bands in phyllosilicates. Zeolites were identified by the presence of absorption bands at 1.9, 1.4 and ~1.75

298   microns. Spectra were not gathered from the thinnest and least developed paleosol (Entisol), but all three
299   paleosol types were subject to X-ray diffraction and evolved gas analysis, discussed below.

2.5 X-ray diffraction of paleosol samples

301   Paleosols were powdered and homogenized to < 45 μm grain size, then unoriented samples were
302   mounted on aluminum holders and measured using a PANalytical X'pert Pro MPD XRD at NASA
303   Johnson Space Center. XRD patterns were collected using an X'celerator detector and Co Kα X-ray
304   source, with a Fe filter to reduce Kβ peak intensities. Samples were analyzed under the following
305   conditions: 45 kV, 40 mA, ½° antiscatter slit, ¼° fixed divergence slit, and a beam knife to reduce low-
306   angle scattering. Samples were measured from 4° to 80° 2θ with a 0.02° step size at 100s/step. Mineral
307   identification was accomplished using HighScore and Jade MDI software by comparing XRD patterns to
308   International Center for Diffraction Data (ICDD) database patterns, and with Crystallography Open
309   Database (COD) patterns.

310   Semi-quantitative XRD (no internal standard) was used to provide a relative estimate of phyllosilicate
311   abundances. Rietveld refinement [59] was carried out using MDI Jade Software with initial structure
312   parameters for crystalline phases from the RRUFF database (http://rruff.info/). Background patterns were
313   fit by a polynomial and peaks were modeled by a pseudo-Voigt profile function. Pattern overlays of
314   standard phyllosilicates with known relative intensity ratio (RIR) and full width at half maximum
315   (FWHM) from the Clay Minerals Society [60] were used in Rietveld refinements to estimate abundances of
316   phyllosilicates in bulk samples. Since no internal standard was used, semi-quantitative XRD was used
317   only for estimating the relative abundances of phyllosilicates in each sample (Table S4).

2.6 Thermal and evolved gas analysis (EGA) of paleosol samples

319   A Setaram Labsys Evo differential scanning calorimeter (DSC) / thermal gravimeter (TG)
320   connected to a Pfeiffer Omnistar quadrupole mass spectrometer (QMS) was configured to operate
321   similarly to the SAM evolved gas analyzer. The Sample Analysis at Mars (SAM) onboard *Curiosity* Mars
322   Rover does not have TG/DSC capabilities, but these components permit a better understanding of phase
323   transitions and chemical reactions in laboratory experiments. Approximately 50 mg ± 3 mg of ground
324   paleosol sample were placed in an Al_2O_3 sample crucible which was previously ashed at 500° C to
325   remove organic contaminants before use. The sample crucible and an identical empty reference crucible
326   were placed in the furnace and then the system was purged twice with helium gas and then set to a
327   pressure of 30 mbar. Helium was chosen as a carrier gas because it is inert and because it used as a carrier
328   gas in the SAM instrument. The crucibles were heated from approximately 35 °C to 1000 °C at a heating
329   rate of 35°C/min and at a flow rate of 10 sccm. Volatiles ranging from mass/charge (m/z) 1 - 100 were
330   measured. All analyses were performed in duplicate.

331   Evolved water abundances were determined using a Netzsch TG/DSC coupled to a Pfeiffer QMS. An
332   Al_2O_3 sample crucible and an identical reference crucible were placed in the furnace. The instrument was
333   purged twice with ultra-high purity O_2 and set to a pressure of 1000 mbar prior to sample analyses to
334   remove any contamination in the system. The crucibles were heated from approximately 35 °C to 1000 °C
335   at a heating rate of 35°C/min and at a flow rate of 19 ml O_2/min. A series of three blanks were analyzed
336   before and after each group (n=10) of samples. A calibration curve for CO_2 was created by analyzing a
337   calcite standard (Iceland sparry calcite 40 ʮM) at eight sample masses ranging from 0.01 – 4 mg. This
338   calibration curve was used to calculate the amount of CO_2 evolved from each sample, and these values
339   were converted to weight percent and subtracted from the thermogravimetric data to estimate mass loss
340   from water evolutions. Oxygen was chosen as a carrier gas because it encourages complete combustion of
341   all organic and inorganic carbon in samples, which indirectly allowed for calculation of evolved water

342 abundances. Since there were no major overlapping gases with evolved water, mass loss from low
343 amounts (< 0.1 wt. %) of organic and inorganic carbon were the only significant sources of mass loss
344 aside from water loss from hydrated phases (~3-5 wt. %), so the remaining mass loss after accounting for
345 CO_2 evolutions was attributed to evolved to H_2O, thus allowing for estimates of evolved water abundances
346 from the thermogravimetric data. All analyses were performed in duplicate.

347
348 **2.7 Bulk geochemistry and grain size**
349   Previously published estimates of bulk geochemistry and grain size were used to augment
350 determination of mineralogy. Retallack et al. (2000) collected oriented paleosol samples for point
351 counting and bulk geochemistry. Point counting (500 points) to determine relative percent of sand, silt
352 and clay size fractions was performed using a Swift automated stage and Hacker counting box fitted to a
353 Leitz Orthoplan Pol research microscope. Accuracy of point counting was determined to be ± 2 wt. % for
354 common constituents. Bulk density was also previously determined by the clod method [18] first by
355 determining raw weight, then weight of clods coated in paraffin of known density (0.86g cm^{-3}) in and out
356 of chilled (6°C) water (1.00 g cm^{-3}). Major element chemistry of paleosols was determined by X-ray
357 fluorescence, atomic absorbance, and X-ray diffraction at Washington State University, Pullman (Table
358 S1). These previously published data were used to calculate chemical index of alteration and molar
359 weathering ratios of each paleosol profile examined in this work. Major element chemistry from Retallack
360 et al. (2000) and calculated CIA and molar weathering ratios are both included as supplementary data
361 (Table S1).

362   **3.   Results and Discussion**
363   **3.1 Chemical weathering trends**

364   Trends in molecular weathering ratios across the three paleosol types were attributed to
365 differences in chemical weathering intensity and duration. All profiles showed evidence of hydrolysis
366 of volcaniclastic sediments from increases in alumina/silica and alumina/bases toward the top of
367 profiles (Figure 4). The clay size fraction ranged from 75.0 to 95.4 ± 2 wt. % and was greatest in the
368 subsurface (Bt) horizon of the Alfisol and lowest in the surface (A) horizon of the Entisol. Generally
369 low ranges of calcification (CaO + MgO/Al$_2$O$_3$) were noted in all three profiles and suggested
370 minimal or absent accumulation of $CaCO_3$. This is characteristic of subtropical to temperate soils
371 receiving annual rainfall of 600-1200 mm[31]. Pedogenic $CaCO_3$ typically accumulates in arid to semi-
372 arid soils where annual evapotranspiration exceeds precipitation [61] and thus significant $CaCO_3$
373 accumulation was unlikely for paleosols from the Big Basin Member of the John Day Formation.
374 There were negligible trends in alumina/silica ratios, but declining trends in Na$_2$O/K$_2$O suggest slight
375 salinization in the uppermost paleosol (Alfisol), although this trend terminated in the surface (A)
376 horizon of the Inceptisol. Salinization, a rough measure of the original salt content of paleosols, is
377 defined by the molar ratio of Na$_2$O to K$_2$O and results from the deposition and/or precipitation of salts
378 in the original soil. Minimal salinization may have caused the slight increase in this ratio at the
379 surface of the Alfisol, but salinization was likely not severe because there was a lack of domed
380 columnar peds and salt crystals that are characteristic of salt-affected soils and paleosols [18,62]. Lack of
381 carbonate and generally deep weathering inferred from high smectite content is consistent with acidic
382 pH, but low alumina/bases ratio, smectite mineralogy and residual feldspar clasts indicate moderate
383 base saturation across all profiles. A pH of ~5.5 -7.5 is characteristic of Alfisols formed in similar
384 climates [29], but diagenetic fluids can alter the original soil pH after burial and lithification, thereby
385 obscuring primary pH values [63]. High oxidation of iron (FeO/Fe$_2$O$_3$ = 0) and deeply penetrating root
386 traces indicate soil formation in well-drained settings, though the surface (A) horizon of the Alfisol
387 showed slight gleyization (FeO/Fe$_2$O$_3$ > 0) most likely from the onset of chemically reducing
388 conditions shortly after burial. This has been attributed to a diagenetic phenomenon known as burial
389 gleization (discussed in detail in Section 3.5) that typically affects the organic matter-rich surface
390 horizons of rapidly buried paleosols.

391　　　　The chemical index of alteration (CIA) ranged from 72.1 to 80.8 and generally decreased with
392　　　depth across the Alfisol and Inceptisol (Figure 4). The highest values (80.8) were in the subsurface
393　　　clay (Bt) horizon of the Alfisol and lowest (72.1) in the C-horizon of the lowermost Inceptisol. The
394　　　CIA in clayey paleosols is generally highest in subsurface horizons due to illuvial accumulation of
395　　　clay minerals during top-down hydrolytic weathering and therefore these horizons are thought to be
396　　　the most reliable for paleoclimate estimations [31]. In contrast, the unweathered, lowermost C and R
397　　　horizons of paleosols (e.g., saprolite) reflect the characteristics of the soil parent material rather than
398　　　alteration from weathering, and thus CIA is lower in these horizons. The thinnest and least developed
399　　　paleosol (Entisol) preserves a parent material of redeposited tuffaceous clayey siltstone that was
400　　　minimally altered by soil formation, inferred from relict bedding in the C-horizon. The high clay
401　　　content of this paleosol (~75 wt. %) was most likely inherited from preexisting soils by sheet erosion
402　　　or flooding. It is unlikely that the Entisol was developed for long enough to develop characteristics
403　　　indicative of paleoclimate, and therefore estimations of CIA are unreliable and not shown.

404
405
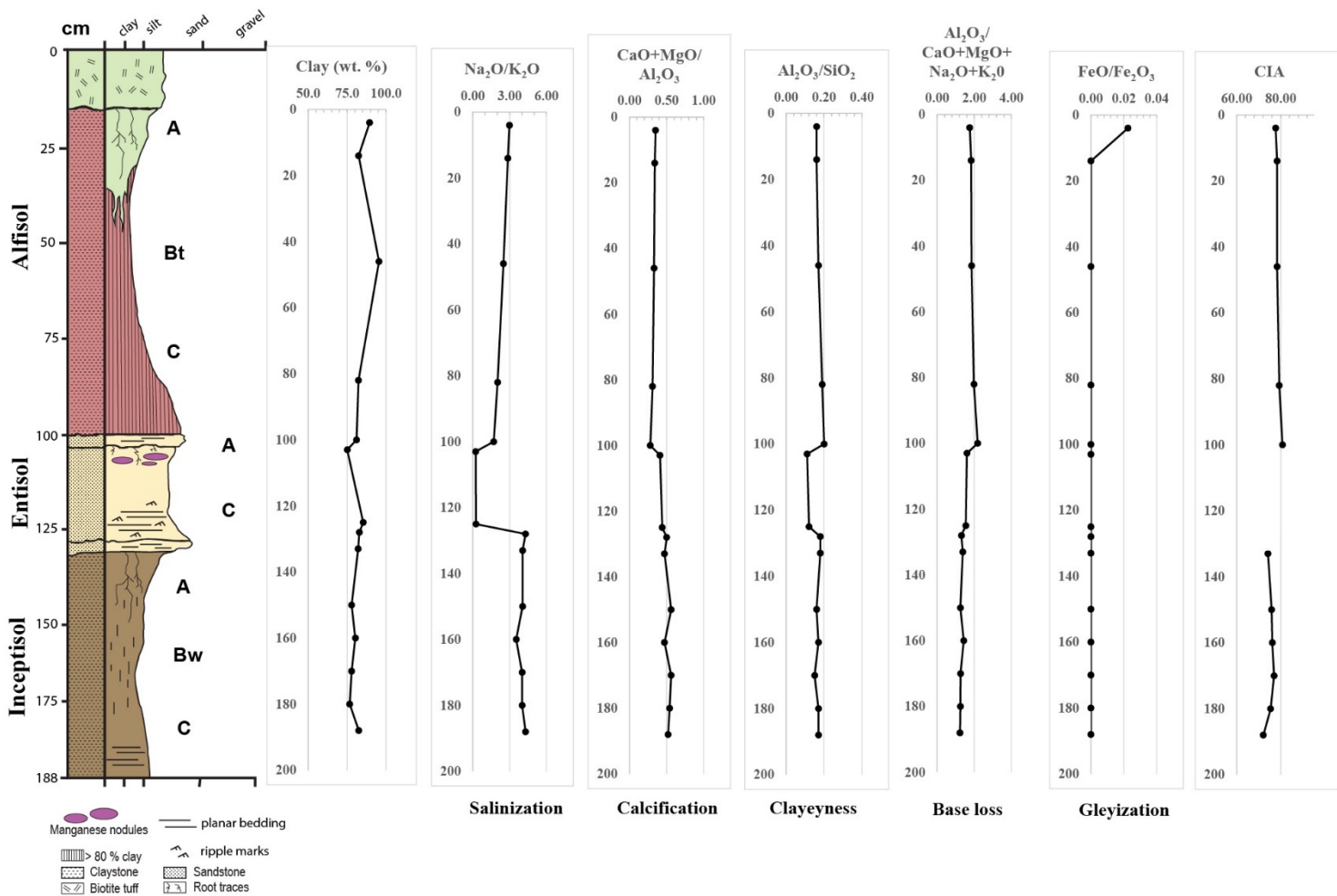
407　　**Figure 4. Chemical weathering trends as a function of depth across three paleosol profiles from**
408　　**the Oligocene (33 Ma) Big Basin Member of the John Day Formation.** CIA = Chemical index of
409　　alteration, not shown for the weakly developed Entisol (middle profile).

410

411   **3.2 Visible/ near infrared spectroscopy of paleosols**
412   The mineralogy of paleosols observed with VNIR spectroscopy was dominated by dioctahedral
413   phyllosilicates and occasionally zeolites and hematite. All paleosol samples had strong spectral signatures
414   of 2:1 Al/Fe dioctahedral smectites (Figure 5) and distinct changes in mineralogy were observed within
415   and between paleosol profiles. Spectral absorption bands were consistent with mixtures of Al-
416   montmorillonite and Fe-nontronite, and/or Fe substitution in montmorillonite. There were no apparent
417   reflectance features characteristic of trioctahedral smectites such as saponite [64] or 1:1 smectites such as
418   kaolin group clays [58].
419   At the stratigraphically highest location, the near-surface horizon of the Alfisol, characterized by
420   a drab green color, showed strong spectral signatures of Al-smectite with an asymmetric doublet feature
421   centered at 2.22 with shoulders at 2.21 and 2.25 μm, and a strong water band at 1.92 μm (Figures 5 and
422   6). Band depths of the 1.9 and 2.2 μm absorption bands were variable across all samples (Supplementary
423   Data). Al smectites such as montmorillonite have a characteristic band at 2.21 μm, but the position of this
424   band varies with Al-Fe-Mg abundance, where substitution of Fe for Al can cause additional bands at 2.23-
425   2.25 μm [58]. A broad absorption band beginning near 2.4 μm was consistent with zeolites such as
426   clinoptilolite. Zeolites are likely also responsible for the strong hydration overtone bands at 0.98, 1.19,
427   1.45, 1.78, and 1.95 μm, of which usually only the 1.4 and 1.9 μm bands are visible in most other
428   hydrated minerals. Diagenetic zeolitization of a poorly crystalline smectite or volcanic glass is thought to
429   have led to the formation of clinoptilolite in paleosols from the John Day Formation [29]. At shorter
430   wavelengths, the sample showed a shoulder at 0.5 μm and a strong band at 0.65 μm due to Fe^{3+} in
431   smectite, as well as a broad weak absorption near 1.1 μm likely due to $Fe^{2+/3+}$ in smectite [40].
432   Stratigraphically lower, the subsurface (Bt) horizon of the Alfisol had much weaker signatures of
433   an Al smectite with minor amounts of Fe-smectite. (Figure 5). Below this sample, the Alfisol C-horizon
434   had a broad absorption band at 0.9 μm attributed to hematite, as well as weak absorption bands of Al
435   smectite similar to the Bt-horizon. The 0.65 and 0.95 μm bands were absent in these samples which was
436   consistent with an absence of Fe-smectite. Hematite in the C-horizon of the Alfisol may have formed
437   from burial dehydration of ferric (oxy)hydroxides (e.g., goethite) which is a common diagenetic alteration
438   in paleosols [18]. Bulk geochemistry of the Alfisol samples indicated lower Fe_2O_3 in the surface horizons of
439   samples relative to subsurface horizons (Table S1) which is consistent with VNIR detections of hematite
440   in subsurface horizons.
441   All samples of the brown colored Inceptisol had spectral signatures of a mixed Al/Fe smectite,
442   with a clear band centered at 2.21 μm, a shoulder at 2.23 μm, and a weak band at 2.29 μm, and no
443   detection of hematite. Strong absorption bands near 1.45 and 1.91 μm and a shoulder at 2.23 μm were
444   consistent with Opal-CT [65]. The light brown Munsell color of this sample (2.5Y 5/2) was markedly
445   different than the brick-red (10R 7/1) color of the overlying Alfisol and suggests hematite abundances
446   were much lower or absent in the Inceptisol. Sharp 0.65 and 0.95 μm Fe smectite absorption bands
447   throughout the profile were consistent with accumulations of nontronite and/or Fe montmorillonite. Like
448   the overlying Alfisol, band depths of the 1.9 and 2.21 μm absorption bands were also variable across all
449   samples in the Inceptisol profile (Table S1).
450
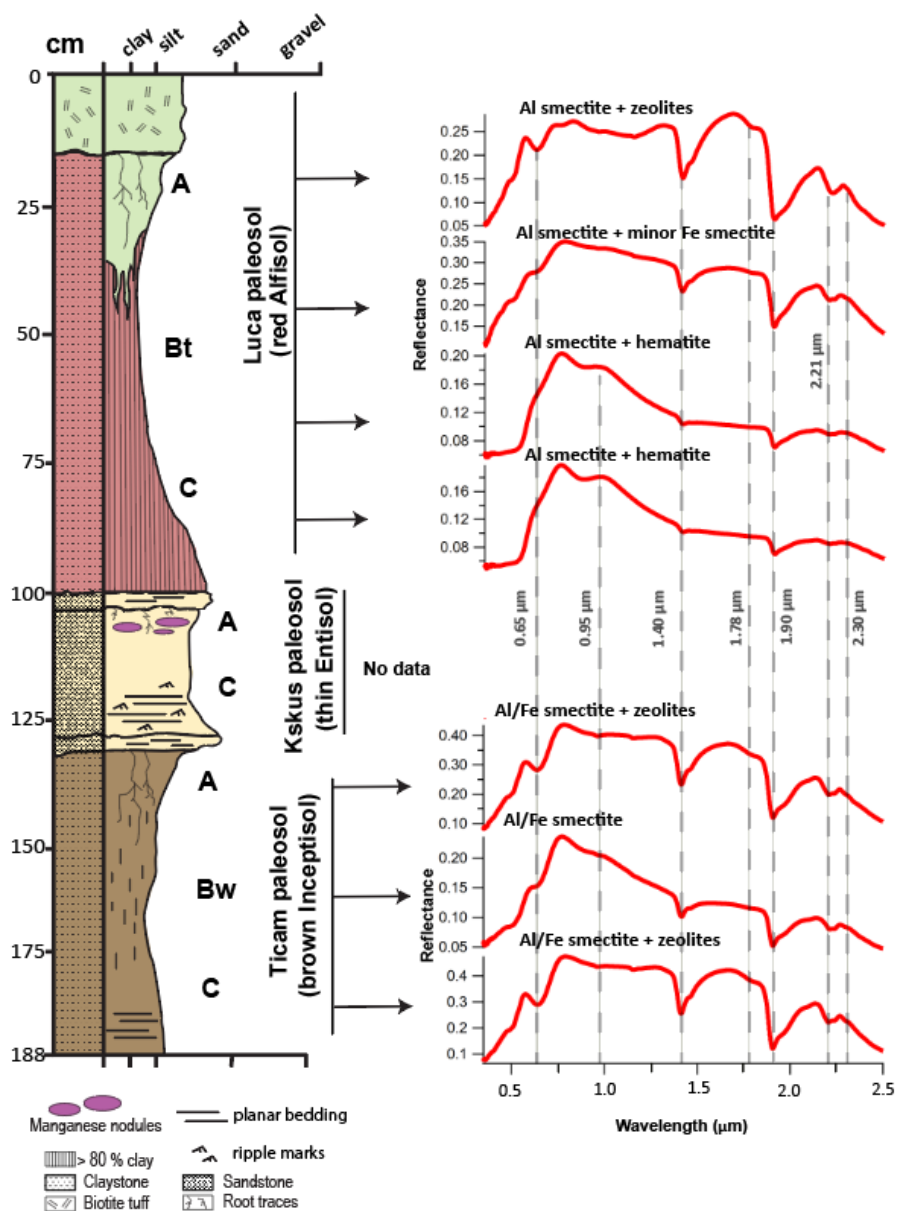
452
453
454   **Figure 5. Visible/near infrared reflectance (VNIR) spectra of two paleosols (Alfisol and Inceptisol)**
455   **from the early Oligocene (33 Ma) middle Big Basin Member of the John Day Formation in eastern Oregon,**
456   **USA**.

457   The spectral "doublet" feature with bands near 2.21 and 2.23-2.25 μm was observed in all
458   samples and was attributed to OH stretching and bending combination vibrations in phyllosilicates
459   (Figure 6). Doublet-type spectra typically represent mixtures of various hydrated minerals including
460   kaolinite, Al-smectites and sulfate minerals [35,66], and previous work has shown that Fe^{2+}/Fe^{3+} smectites
461   exhibit bands in this region [64]. A doublet feature near 2.21 and 2.23-2.25 μm may be a unique
462   spectroscopic feature of pedogenic smectites that results from isomorphous substitution in the tetrahedral
463   layer of 2:1 phyllosilicates during subaerial weathering. Previous work on smectite-rich mafic soils and
464   paleosols show similar doublet features between 2.2 and 2.3 μm that are absent in standard clays [58,67]. The

465 position and shape of the bands is highly variable, which may result from the isomorphic substitution of
466 large amounts of Fe for Al which presumably distorts the crystal structure of clay minerals formed in
467 mafic soils. These doublet features noted in paleosol samples here are similar to doublet features
468 previously observed in paleosols from the John Day Formation [67]. Thus, the doublet features here are
469 consistent with a pedogenic origin for Fe/Al smectites as has been previously suggested [67], though it
470 should be noted that the phyllosilicate doublet feature has not been observed in silicic soils or other
471 phyllosilicate-rich rocks [50,68], so absence of the feature is not necessary evidence against a pedogenic
472 origin for clay minerals.
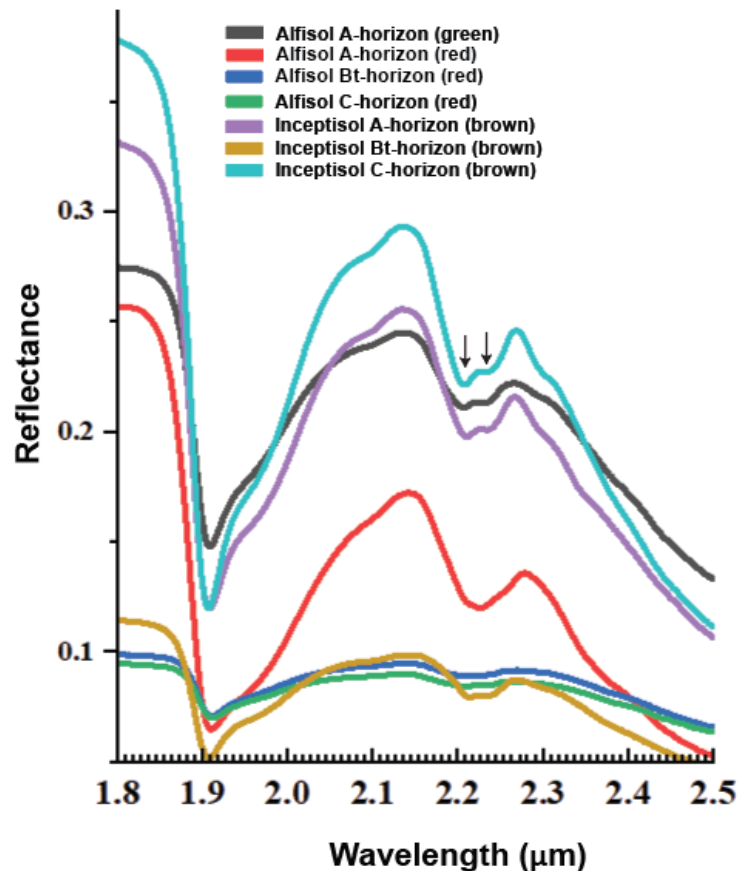
474 **Figure 6. Near-infrared spectra from surface and subsurface horizons of two paleosols (Alfisol and**
475 **Inceptisol) from the early Oligocene (33 Ma) middle Big Basin Member of the John Day Formation**. Spectral
476 doublet feature between 2.2 and 2.23-2.25 µm is indicated with black arrows.

477
478
479 **3.3 X-ray diffraction of paleosols**
480 XRD diffractograms showed strongly crystalline clay minerals dominated all samples (Figure 7,
481 Table 1). Major phases identified in all samples (> 5 wt. %) were montmorillonite (Al smectite) and
482 nontronite (Fe smectite) while minor phases (< 5 wt. %.) identified from patterns in all samples were
483 clinoptilolite, cristobalite, Opal-CT, quartz, andesine, orthoclase, gypsum and jarosite. Notably, the
484 zeolite mineral clinoptilolite ($Na_{.66}Ca_{.86}K_{.64}Mg_{.26}Si_{18}O_{49.42}H_{26.4}$) was identified from patterns in all
485 paleosol samples, which likely formed from post-burial alteration of volcanic glass or other poorly
486 ordered phases including smectite during Miocene-age burial recrystallization [29].
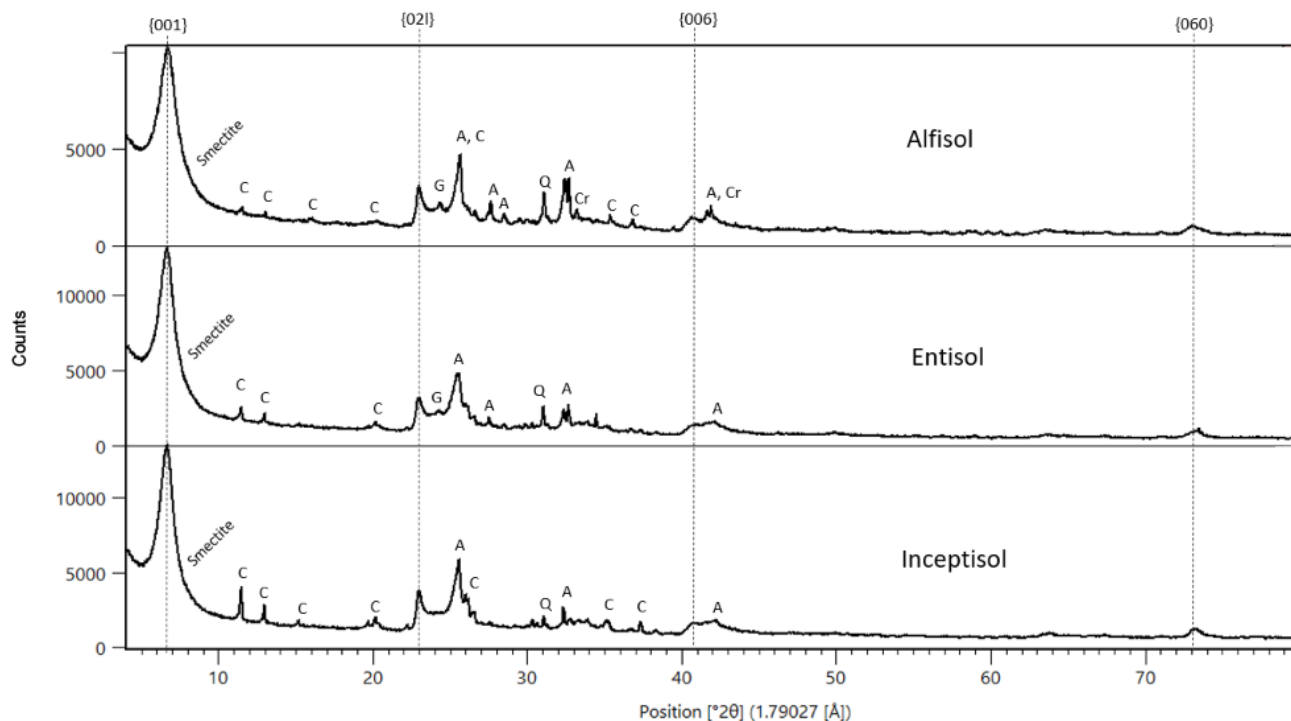
488 **Figure 7. X-ray diffraction patterns from the near surface (A-horizon) of three paleosols from the early**
489 **Oligocene (33 Ma) middle Big Basin Member of the John Day Formation in eastern Oregon, USA.**
490 **S=Smectite; G=Gypsum; A=Andesine; C=Clinoptilolite; Cr=Cristobalite; Q=Quartz.** Highlighted are the 001
491 and 02l smectite peaks; difference in 02l band position corresponds to a difference in octahedral occupancy.

492   Beginning with the stratigraphically highest sample (Alfisol 4 cm), major phases identified from
493 patterns were montmorillonite and nontronite while minor phases identified were andesine, Opal-CT and
494 cristobalite, with lesser abundances of clinoptilolite, quartz, gypsum, jarosite, and anatase (Figure 7).
495 Stratigraphically below this sample, the Alfisol A-horizon at 14 cm showed a similar mineral assemblage
496 with the addition of albite as a minor phase (Table 1). A deeper sample of the Alfisol at 46 cm (Bt
497 horizon) had montmorillonite and nontronite as major phases and albite, cristobalite, opal-CT,
498 clinoptilolite, hematite, quartz and anatase as minor phases. Directly below, the pattern from Entisol A-
499 horizon at 7 cm was consistent with montmorillonite and nontronite as major phases and cristobalite,
500 anatase, clinoptilolite, and orthoclase as minor phases (Figure 7). Stratigraphically below this sample, the
501 pattern for the near-surface (A) horizon of the Inceptisol (3 cm) showed montmorillonite, nontronite and
502 Opal-CT as major phases and clinoptilolite, cristobalite, andesine, orthoclase, quartz, and gypsum as
503 minor phases. The pattern from the stratigraphically lowest sample, the Inceptisol Bw-horizon at 21 cm,
504 showed the same major phases as the A-horizon (3 cm) sample, but with the additions of hematite,
505 ilmenite ($FeTiO_3$) and anatase along with clinoptilolite, cristobalite, quartz and andesine as minor phases.

506 **Table 1. Summary of major and minor phases detected with x-ray diffraction.** Major phases (> 5 wt.
507 % are noted with an X while minor phases (< 5 wt. %) are noted with an asterisk.

	Alfisol (4 cm)	Alfisol (14 cm)	Alfisol (46 cm)	Entisol (3 cm)	Entisol (7 cm)	Inceptisol (3 cm)	Inceptisol (7 cm)	
Montmorillonite	X	X	X	X	X	X	X	
Nontronite	X	X	X	X	X	X	X	
Saponite			*					
Andesite		X				*	*	
Clinoptililite		*		*	*	*	*	
Cristobalite	*	*	*	*	*	*	*	
Opal-CT	*	*	*	X	X	X	X	
Quartz	*	*	*	*	*	*	*	
Anatase	*	*	*	*	*	*	*	
Albite		X	X	*	*			
Orthoclase					*	*	*	
Hematite			*				*	
Gypsum	*		*	*	*	*	*	
Jarosite	*							
Others/Amorphous				*	*	*	*	

509   The abundance of crystalline clay minerals across all samples is consistent with pedogenic
510 surface weathering of andesitic to rhyolitic tuff / ash under a temperate climate (MAT of ~10° C and
511 MAP of 600-1200 mm) over 10-100 Kyr of soil formation [29]. This agrees with other estimates of MAT
512 > 12° C and MAP of > 1000 mm from geochemical climofunctions applied to the subsurface horizons
513 of paleosols from the middle Big Basin Member (~33.7 Ma) of the John Day Formation [31]. This amount
514 of surface weathering over tens to hundreds of thousands of years transformed most volcanic glass to
515 smectite via hydrolytic weathering, potentially leaving only a small x-ray amorphous component (e.g.,
516 unweathered volcanic glass and/or poorly ordered phases) which presumably was diagenetically altered
517 via zeolitization to clinoptilolite. There were no XRD detections of illite which suggests minimal or
518 absent potash metasomatism despite burial by an estimated ~2 km of overburden [69].
519

520 **3.4 Evolved Gas Analysis**
521 **3.4.1 H_2O evolutions**
522   All samples evolved H_2O (m/z 18) during evolved gas analyses which was attributed to the
523 release of adsorbed water, interlayer water, and water from dehydroxylation in the octahedral layer of a
524 dioctahedral clay mineral (Figure 8). Low temperature (< 450 °C) and high temperature (>450 °C)
525 evolutions of water from paleosol samples co-occurred with an endotherm in the heat flow data (dotted
526 line, Figure 8) resulting from endothermic dehydration and dehydroxylation reactions, respectively.
527 Evolved water abundances ranged from 3.24 ± 0.47 wt. % to 5.03 ± 0.12 wt. % H_2O across all samples (n
528 = 20) and trends in water abundances were apparent across the three paleosols. The Alfisol evolved the
529 lowest amount of water observed with 3.24 ± 0.47 in the subsurface (Bt) horizon whereas the Entisol
530 averaged 5.03 ± 12 wt. % which was the highest amount of evolved water observed in the experiment.
531 The Inceptisol ranged from 4.32 ± 0.03 wt. % to 4.81 ± 0.13 wt. % H_2O and showed a trend of decreasing
532 abundance with depth. Despite significant differences in evolved water abundances between profiles, each
533 profile generally showed a decrease in evolved water abundance with depth. Though many factors control
534 the abundance and persistence of hydrated phases in paleosols, trends in evolved water abundances could
535 have resulted from lateral and vertical diversity in mineralogy within each of the paleosol profiles.
536   Water evolutions at temperatures less than 300 °C were consistent with adsorbed water on
537 mineral surfaces [70]. Evolutions of H_2O between 100 °C and 300 °C can result from the release of
538 interlayer H_2O from smectite and other 2:1 clay minerals (McAdam et al., 2020) or from dehydroxylation
539 and/or dehydration of poorly crystalline, nanophase or amorphous aluminosilicates such as allophane and
540 imogolite [72]. Nanophase oxides/oxyhydroxides including ferrihydrite can evolve adsorbed H_2O at
541 temperatures ranges below ~450 °C due to their high specific surface areas [73] and could have contributed
542 to water evolutions below 200 °C. Other sources of minor H_2O evolutions near 300 °C could be from
543 oxyhydroxides such as goethite which dehydroxylate at temperatures ranging from 280-320 °C [74].

544 Differences in evolved H_2O peaks < 450 °C across the three paleosols examined here may have
545 resulted from differences in abundance and composition of x-ray amorphous components. Though
546 amorphous phase composition was not examined in this work, a previous study identified basaltic glass
547 (5.6 wt. %), allophanes (7.9 wt. %) and ferrihydrite (0.6 wt. %) as the dominant amorphous phases in
548 paleosols from the Oligocene (~28 Ma) Turtle Cove member of the John Day Formation (Smith et al.,
549 2018) which are stratigraphically higher than paleosols examined here (Figure 1). Turtle Cove paleosols
550 have mineralogical and paleobotanical evidence of a cool and dry climate of an estimated MAP of 400–
551 600 mm (Figure 2) and thus minor alteration of volcanic ash and tuff [31]. A SAM-EGA analog analysis of
552 a Turtle Cove paleosol was performed by Smith et al. (2018) [72] who noted a water release peak at ~290 °C
553 which was attributed to the abundance (> ~40 wt. %) of amorphous materials in the sample, unlike the
554 low amount (< 5 wt. %) of x-ray amorphous phases found in smectitic paleosols in the middle Big Basin
555 member of the John Day Formation. Paleosols from the Big Basin Member formed under a much warmer
556 (MAT 16-18° C) and wetter (MAP 600-1200 mm) climate than those from the Turtle Cove Member and
557 was sufficient to transform amorphous and nanocrystalline phases to Al/Fe smectites. In the present study
558 there were no sharp water release peaks at ~290 °C (Figure 8), possibly because samples are composed
559 primarily of strongly crystalline clay minerals rather than amorphous colloids, especially the Alfisol with
560 up to 95 wt. % clay minerals (Figure 3). However, a minor 300 °C endotherm in all samples is consistent
561 with small amounts of amorphous phases, which were also detected with XRD as minor phases in the
562 Entisol and Inceptisol (Table 1). In contrast to the moderately weathered Alfisol, the Entisol and
563 Inceptisol were only minimally weathered before burial, inferred from morphological features such as
564 absence of clay illuviation and persistence of relict bedding in subsurface horizons (Figure 3). As such,
565 differences in the duration of weathering before burial can explain the persistence of amorphous phases in
566 the Entisol and Inceptisol and absence of amorphous phases in the Alfisol.
567 Overall, the preservation of metastable amorphous phases over geological time scales is
568 uncommon in sedimentary rocks; however, recent work has shown that large amounts (> 40 wt. %) of
569 amorphous colloids have persisted for millions of years in lithified and diagenetically altered
570 volcaniclastic paleosols from the Oligocene (~28 Ma) Turtle Cove Member of the John Day Formation [19].
571 Thus, detections of minor amounts of amorphous phases (< 5 wt. %) with both EGA and XRD suggest
572 metastable amorphous and/or nanocrystalline phases may have also persisted for ~33 Ma in paleosols
573 from the middle Big Basin Member of the John Day Formation.
574
575
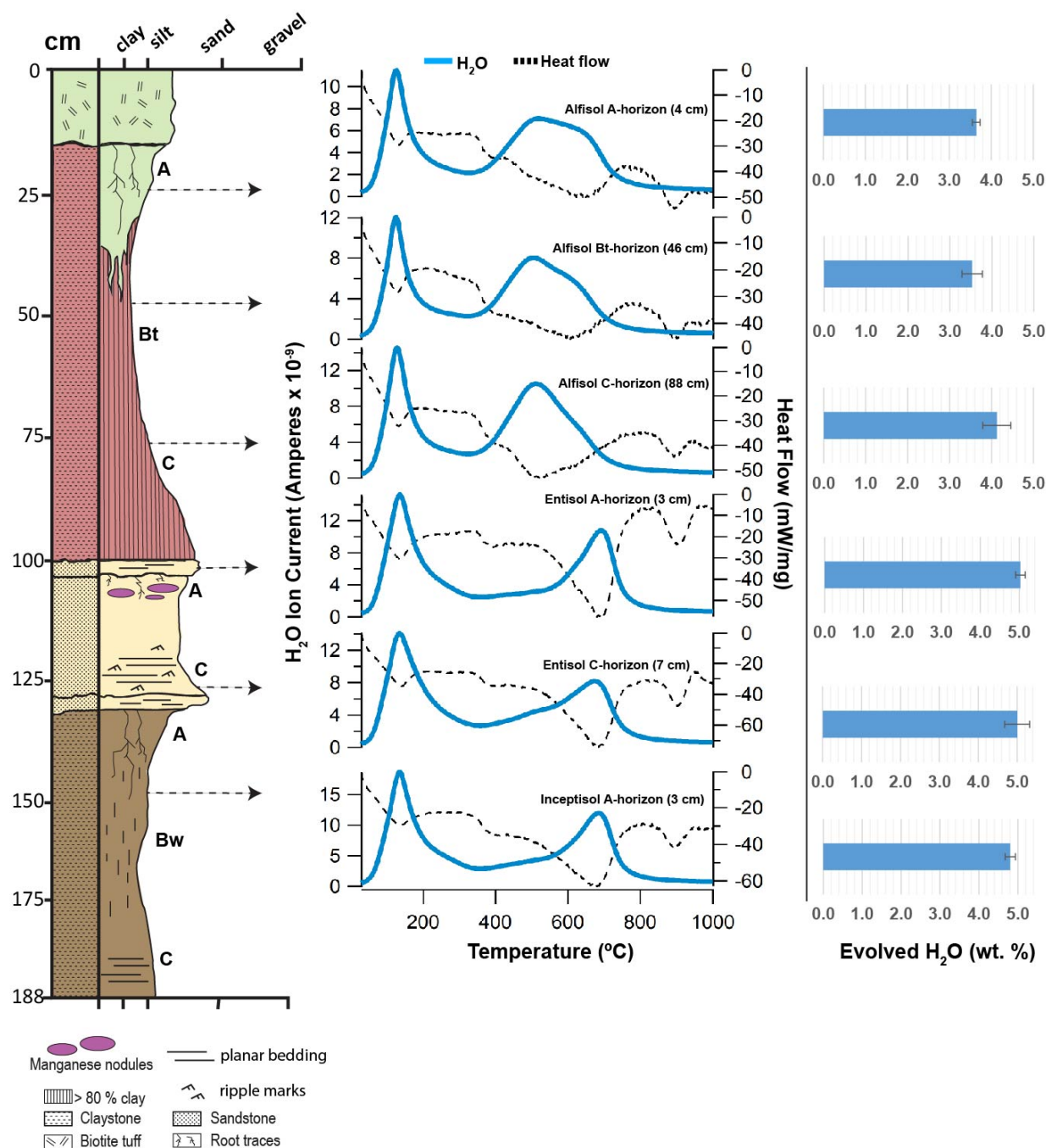
577
578 **Figure 8. Evolutions of H₂O from early Oligocene (33 Ma) paleosols from the John Day Fossil Beds National**
579 **Monument, Oregon.** Blue trace is H_2O (m/z 18), and dashed trace is heat flow from differential scanning
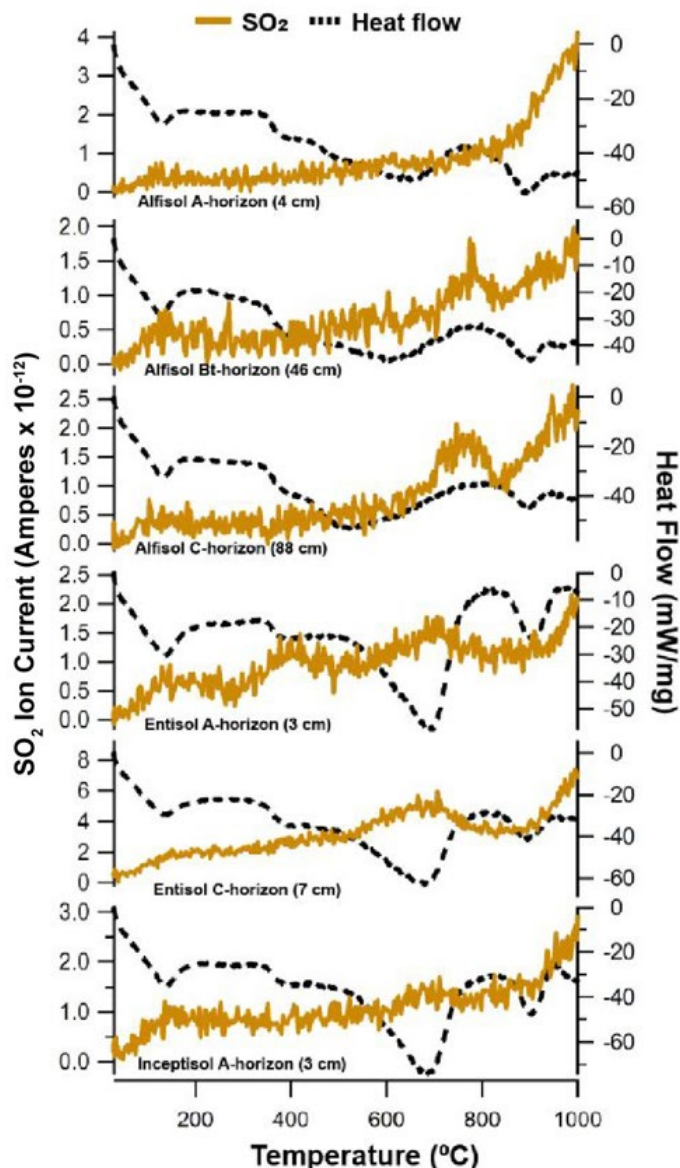580 calorimetry (DSC).
581
582   Evolutions of H_2O above 450° C are consistent with the dehydroxylation of the octahedral layer
583 of a 2:1 phyllosilicate [71,75], and there was a ~200° C difference in H_2O peak release temperature between
584 the three paleosols. The Alfisol with ~95 wt. % smectite evolved H_2O with peaks centered at ~500° C,
585 while the Entisol (~75 wt. % smectite) and the Inceptisol (~78 wt. % smectite) evolved H_2O with peaks
586 centered at ~ 700 °C. Differences in clay mineralogy between the soils may be responsible for shifting the

587   peaks and shoulders of the high-temperature (> 450° C) evolutions. The considerable difference in peak
588   H_2O release temperature between the red Alfisol (~500° C) and the other soils (~700° C, Figure 8) could
589   have resulted from differences in the occupation of the octahedral sheet of a 2:1 phyllosilicate [70] which
590   leads to differences in the high temperature H_2O peak release temperature during SAM-EGA [76,77]. Clay
591   minerals with Fe in the octahedral layer (e.g., nontronite or Fe-montmorillonite) dehydroxylate at a lower
592   temperature (~500° C) relative to smectite with Al in the octahedral layer (e.g., Al-montmorillonite, 700°
593   C) [77], though mixed illite-smectite mineralogy also show peak H_2O release at 698° C. The Alfisol (~500°
594   C peak H_2O release) exhibited strong VNIR signatures of an Al-smectite with minor Fe-smectite and
595   hematite. The brown Inceptisol (~700° C peak H_2O release) had strong VNIR signatures of an Al/Fe
596   smectite and lacked hematite (Figure 5). Differences in clay mineralogy across the samples likely caused
597   the large difference (~200° C) of peak water release temperatures from smectite dehydroxylation.
598   Together these results show that EGA in conjunction with XRD and VNIR spectroscopy are suitable
599   techniques to constrain smectite mineralogy in paleosols.
600
601   **3.4.2 SO_2 evolutions**
602   All samples evolved minor amounts of SO_2 primarily above 450° C (Figure 9). Minor SO_2 peaks
603   below 400° C were observed in the Bt-horizon of the Alfisol and the A-horizon of the Entisol (Figure 9)
604   which most likely resulted from instrument background sources. A distinct SO_2 peak at 400° C in the A-
605   horizon of the Entisol is consistent with the presence of minor amounts of sulfides such as pyrite and/or
606   pyrrhotite which thermally decompose at temperatures above 400° C under SAM-EGA analog conditions
607   [78]. Oxidative sulfite decomposition directly to SO_2 could have resulted from trace amounts of oxygen in
608   the instrument furnace even after successive purges with helium and are the likely source of the broad
609   400° C SO_2 peak noted in the Entisol.

611 **Figure 9. Evolutions of SO₂ from early Oligocene (33 Ma) paleosols from the John Day Fossil Beds National**
612 **Monument, Oregon.** Yellow trace is SO₂ (m/z 64), and dashed trace is heat flow from differential scanning
613 calorimetry (DSC).
614
615 Evolutions of SO_2 above 500° C are consistent with the thermal decomposition of Ca and Fe
616 sulfates ranging from crystalline (gypsum and jarosite) to amorphous and/or adsorbed sulfate [73,78]. Also
617 possible are contributions from organo-sulfur compounds and/or S phase inclusions in volcanic glass.
618 Crystalline sulfate species including jarosite and gypsum have peak SO_2 release temperatures near 900° C
619 and 1200° C, respectively [74]. Thus, jarosite and gypsum most likely account for the evolutions of SO_2
620 above 600° C and both were confirmed as minor phases with XRD (Table 1). Samples from the Bt and C
621 horizons of the Alfisol had a broad SO_2 release with a peak at ~790° C that was absent in the Entisol and
622 Inceptisol. Trace amounts of Mg sulfates in the Alfisol could account for minor SO_2 releases > 700° C
623 including the ~790° C SO_2 peaks [71,79] At higher temperatures, all soils showed a major release of SO_2
624 beginning at 900° C which co-occurred with an endotherm, both of which are consistent with the thermal

625 decomposition of crystalline sulfates [75,79]. Since the samples were only heated to ~1000° C for this work,
626 the maximum peak height of this release cannot be ascertained.
627   The presence of sulfate minerals is uncommon in smectite-rich soils such as those examined here.
628 Sulfate minerals such as gypsum and jarosite tend to form at low pH and low water:rock ratios whereas
629 pedogenic smectites such as montmorillonite typically form at circumneutral pH and increased water:rock
630 ratios. Both gypsum and jarosite are unlikely to be original minerals in the paleosols, but more likely
631 formed in the current weathering zone. One possibility for the origin of sulfate minerals in these paleosols
632 is leaching from the modern soils forming atop paleosols (e.g., the weathered paleosol surface). These
633 modern soils that mantle paleosol outcrops have visibly accumulated pedogenic gypsum into a thin (~1
634 cm) subsurface gypsic (By) horizon, allowing for their classification as Gypsids (gypsum-rich desert
635 soils) in US Soil Taxonomy[32]. The modern soils are subject to an estimated MAT of 33° C and MAP of
636 290 mm which is significantly warmer and drier than the estimated conditions during the formation of
637 John Day Formation paleosols (MAT 16–18° C and MAP of 600–1,200 mm). Sulfate minerals observed
638 with XRD and EGA could have accumulated over time in the underlying paleosols and therefore it is
639 likely that the modern Gypsic soils forming atop paleosol outcrops are the source of sulfate minerals
640 observed here.
641
642 **3.5 Diagenetic Alteration**

643   Diagenetic alterations, or alterations after burial, are common in paleosols. By definition, soils are
644 an early diagenetic alteration because water-rock interactions during pedogenesis alters the physical and
645 chemical properties of sediments. After burial, however, soils are subject to additional early and late
646 diagenetic alterations ranging from minor (e.g., decomposition of organic matter) to severe (e.g.,
647 metamorphic alteration). Four types of alteration after burial that have affected paleosols examined in this
648 work are 1) Drab olive-green surface horizons attributed to burial gleization; 2) brick-red color from
649 burial-induced dehydration of ferric hydroxide minerals; 3) zeolitization of volcanic glass and/or poorly
650 crystalline phases; and 4) significant mechanical compaction.
651   Burial gleization, also known as gley overprinting [80], has been envisaged as the chemical
652 reduction of iron oxides and hydroxides by anaerobic bacteria in the near-surface horizons of paleosols
653 and is thought to occur shortly after soil burial[81,82]. Burial gleization is an early diagenetic process in
654 paleosols which involves the reduction of Fe^{3+} to Fe^{2+} in clays, oxides and other minerals after rapid
655 burial, and promotes anaerobic decay of organic matter[18], even in soils that originally formed under
656 oxidizing conditions before burial. Typical burial gleization is closed system alteration, without depletion
657 of total iron, and is usually limited to the surface (A) horizons where organic matter is most concentrated.
658 The surface (A) horizon of the uppermost paleosol (Alfisol) examined in this work showed classic
659 evidence of burial gleization with drab-colored mottles and tubular features predominantly in the A-
660 horizon with minor radiation downward into the subsurface (Bt) horizon (Figure 3) as well as
661 accumulations of Fe^{2+} exclusively in the A-horizon (Table S1). Spectroscopic techniques such as VNIR
662 employed here can readily identify burial gleization by observing absorbance features attributed to Fe^{2+} in
663 the surface horizons of paleosols. This was presumably the cause of the broad 1.1-micron Fe^{2+} band in the
664 surface of the Alfisol, and the shoulders at 2.23-2.25 microns noted in the gleyed surface horizon of the
665 Alfisol (Figures 5 and 6).
666   Burial gleization can be distinguished from other original redoximorphic features such as
667 groundwater alteration because it is limited to the surface (A) horizon unlike the gleyed subsurface (Bg)
668 horizons of seasonally or perennially waterlogged soils, and because the mineralogy and morphology of
669 this soil provide evidence of well-drained and oxidizing conditions during soil formation. Morphological
670 evidence of burial gleization in paleosols is a drab greenish-gray color exclusively in near-surface
671 horizons directly below the burial contact[82]. Geochemical evidence of burial gleization can include
672 depletions of Fe^{3+} coupled with increases in Fe^{2+} and the formation of siderite and pyrite. Most soils
673 accumulate organic matter in near-surface horizons, which after burial and the onset of anoxic conditions
674 is generally the horizon most affected by burial gleyization. Though the timing of burial gleization

675   remains poorly constrained, reduction haloes around buried organic matter such as roots can form in tens
676   to hundreds of years after burial[83]**.** In the Alfisol, burial gleyization can be distinguished from
677   groundwater alteration because it is limited to the surface horizon directly below the white biotite-bearing
678   tuff layer which buried the uppermost soil (Figure 3). The original color of the surface horizon of the
679   Alfisol was most likely brown and darkened by accumulation of organic matter. Burial gleization thus
680   indicates the surface horizon of the Alfisol may be enriched in organic matter relative to unaffected
681   subsurface horizons (Bt and C horizons), but burial degradation of organic carbon over geological time
682   scales has likely reduced the original organic carbon content by up to two orders of magnitude [43].
683   Directly below the drab surface horizon, the remainder of the Alfisol profile was brick-red in
684   color (Figure 3, Munsell 10R 3/1) which most likely resulted from dehydration of iron oxyhydroxides [84].
685   This phenomenon, also known as "burial reddening", is one of the most common types of diagenetic
686   alteration in the fossil record of soils on Earth [18,81]. Diagenetic dehydration of oxyhydroxides such as
687   goethite and ferrihydrite forms strongly crystalline hematite which leads to reddening of soils that are
688   originally brown or yellow in color; however, there is little information about the specific temperatures
689   and pressures at which dehydration reactions occur [84]. Such a deep red color is unlikely to be the original
690   color of the Alfisol because comparable modern Alfisols with smectite mineralogy are brown to yellow in
691   color [31]. Brown and yellow weakly to moderately developed Eocene paleosols from Antarctica also have
692   deep red hues attributed to burial dehydration of ferrihydrite and goethite [84]. Some of the kaolinitic and
693   lateritic paleosols in the Clarno and lower John Day Formations show evidence of deep weathering
694   comparable to modern tropical soils that are red in color; however, soils that are not so deeply weathered
695   such as the Alfisol examined here also have a brick-red color which is consistent with burial reddening.
696   Other factors which cause reddening of paleosols include heating by lava flows [85] which can also cause
697   iron oxyhydroxides to dehydrate to hematite and maghemite, but the effects of reddening are typically
698   limited to the near-surface horizons due to the thermal insulation properties of soils [86]. Another possibility
699   is that the protolith of the soil was red in color, but relict bedding and volcanic shards in the subsurface
700   (C) horizon (Figure 3) imply a tuffaceous parent material unlikely to be red in color.
701   The presence of clinoptilolite detected with XRD in all samples (Table 1) suggests zeolitization
702   has pervasively altered paleosols from the John Day Formation. Though zeolites can form in alkaline
703   volcanic soils [87], a diagenetic origin for clinoptilolite is likely because zeolites are commonly destroyed
704   by hydrolysis during original soil formation, especially in the case of the moderately weathered, smectite-
705   rich Alfisol. There are two proposed mechanisms of zeolitization to the John Day Formation paleosols.
706   First, the aqueous flushing model by Hay (1963) [88] proposed that volcanic glass in the lower John Day
707   Formation was diagenetically altered to zeolites by open-system interactions with groundwater that added
708   Ca and H_2O while removing Si, Na and K. Zeolitization may have occurred during early Miocene deep
709   burial at depths of 380-1200 meters and temperatures of 27-55° C during deposition of the overlying
710   Mascall and Rattlesnake Formations. Though the timing of zeolitization is well constrained, the
711   mechanism of alteration by aqueous flushing is not likely because many silty tuff beds in the John Day
712   Formation escaped zeolitization while the clay mineral-rich paleosols did not [29]. These permeable silty
713   tuff beds would have presumably been channels for groundwater, but they include both zeolitized and
714   non-zeolitized segments along strike, suggesting a more localized or patchy distribution of zeolitized
715   facies. These observations are consistent with the hypothesis that some tuffs and paleosols were subject to
716   zeolitization, while others were not.
717   Rather than zeolites forming from groundwater alteration, diagenesis may have been more localized
718   and the formation of clinoptilolite may have instead resulted from burial-induced recrystallization of
719   amorphous colloids and/or volcanic glass [89,90]. The "burial ripening" model of Retallack (2000) [29] for
720   zeolitization of paleosols is supported by observations of only small differences between abundances of
721   alkali and alkali earths in paleosols most altered by zeolitization (the Turtle Cove Member paleosols)
722   when compared with minimally altered tuffs. The stepwise increase in alkali and alkali earths in paleosols
723   from the lower John Day Formation to the upper Turtle Cove Member most likely resulted from decreases
724   in weathering intensity during climatic cooling and drying and is independently supported by soil
725   morphological and paleobotanical evidence of cooling and drying[28,29]. Altogether these lines of evidence

726 support the ripening model for zeolitization which led to localized formation of clinoptilotile from burial-
727 induced crystallization of volcanic glass and/or amorphous colloids. The mechanism(s) of zeolitization
728 are important for interpreting paleosols of the middle John Day Formation including those examined here
729 because their chemical composition would be pervasively altered by the aqueous flushing model, whereas
730 by the burial ripening model their original chemical composition would not have been significantly
731 altered [29].
732   Paleosols from the lower John Day formation are buried by approximately 2 kilometers of overburden
733 which has led to significant mechanical compaction. Burial of soil most often results in compaction of
734 void spaces, fossils and pore water. In clayey soils such as those examined here, compaction of originally
735 loose soil peds creates a complex pattern of slickenslides with random orientation that resembles
736 slickenslides in modern smectitic soils with high shrink-swell capacity (Vertisols in US Taxonomy).
737 Paleosols from the John Day Formation are geologically young enough to allow for comparisons with
738 standard compaction curves for sedimentary rocks. Individual profiles from the middle Big Basin
739 Member are covered by an additional 499 m of John Day formation, 305 m of Columbia River Basalt, up
740 to 605 m of Mascall Formation, and 244 m of Rattlesnake Formation. From this overburden, compaction
741 of paleosols can be estimated using the compaction curve of Sclater and Christie (1980)[91] and are
742 compacted to an estimated ~70% of their original thickness, which would suggest an original thickness of
743 about 1.3 m for the uppermost Alfisol profile, 0.4 m for the Entisol profile, and 1.3 m for the lowermost
744 Inceptisol profile.
745
746 **3.6 Implications for Mars**
747   Paleosols at the John Day Fossil Beds National Monument have been proposed to be comparable
748 with putative weathering profiles on Mars because of similarities in mineralogy, morphology and
749 stratigraphy [15,20,26,43]. These sedimentary rocks can be used to help interpret the alteration history of
750 sedimentary rocks on Mars. Work on terrestrial paleosols presented here have implications for a)
751 interpreting orbital remote sensing data for the pedogenic/diagenetic history of sedimentary rocks on
752 Mars, b) constraining climate and habitability from Martian weathering profiles, c) interpreting *in-situ*
753 results from Martian weathering profiles, and d) biosignature preservation in paleosols.
754
755   Orbital VNIR spectra can be compared with VNIR spectra from terrestrial paleosols to evaluate
756 the pedogenic and diagenetic history of ancient sedimentary rocks on Mars. *In-situ* VNIR spectroscopy of
757 multiple individual paleosol profiles presented here provides a reference frame for evaluating a pedogenic
758 alteration hypothesis for ancient sedimentary rocks on Mars. Though pedogenic processes may have been
759 ubiquitous across the surface of early Mars [6], it is currently unclear from orbital VNIR spectroscopy if
760 weathering sequences formed from continuous pedogenic alteration (e.g., a deep weathering profile) [24,51],
761 or if multiple episodes of alteration followed by burial occurred (e.g., repeated episodes of volcanic ash
762 deposition, subaerial weathering, and burial) [14]. The latter formation mechanism is characteristic of
763 paleosol sequences that are composed of hundreds of individual paleosol profiles [18] such as the Oregon
764 paleosol sequence examined in the present study. At Mawrth Vallis, meter-scale relict bedding of the
765 middle (α2) Al-smectite stratigraphic unit at Muara Crater [24] is consistent with a paleosol sequence
766 hypothesis, though previous work has considered this unit part of a single, massive (~200 m-thick) deep
767 weathering profile [24]. However, the apparent relict bedding of dark-toned layers in the α2 unit [38] would
768 presumably be destroyed if the entire deposit was a deep weathering profile. Vertical changes in
769 mineralogy at Muara Crater are consistent with changes in climate, weathering intensity and geochemistry
770 rather than top-down leaching of acidic and reducing fluids through hundreds of vertical meters of
771 stratigraphy. Furthermore, the resolution of CRISM poses challenges for distinguishing between a
772 paleosol sequence and a deep weathering profile. The orbital remote sensing resolution of CRISM
773 (typically 18 m/ pixel) [5] is much coarser compared to our *in-situ* VNIR observations (sub-meter scale),
774 which perhaps makes groups of individual paleosol profiles appear as "units" with similar mineralogy.
775 Observations of the Oregon paleosol sequence suggest that changes in climate (e.g. Eocene-Oligocene
776 cooling and drying) led to stratigraphic changes in mineralogy rather than the intense and uninterrupted

777 leaching that is characteristic of a deep weathering profile. Instead, the Oregon paleosol sequence reflects
778 a cycle of continuous soil formation and burial that occurred during ~15 million years of climate change.
779 These changes are reflected in the tens of individual paleosol profiles composing the basal Fe/Mg
780 smectite and oxide unit (Clarno Formation, Figure 1) that are overlain by hundreds of individual profiles
781 with Al/Fe smectite mineralogy in the middle unit (Big Basin Member, John Day Formation) which are
782 subsequently overlain by hundreds of profiles dominated by nanophase/amorphous Al and Si materials,
783 hydrated silica, calcite and celadonite in the upper unit (Turtle Cover Member). This type of climate
784 change and repeated soil formation may explain the compositional stratigraphy at Muara Crater, which
785 currently stands as the best example of a putative paleosol sequence on Mars.
786   The examination of Mars-analog paleosols presented here can also help interpret the nature of
787 aqueous alteration of rocks by future rover missions. Data from *in-situ* investigation of putative Mars
788 weathering profiles can be compared to spectral and morphological features observed in this study to
789 constrain the pedogenic and diagenetic history. Pedogenic features observed in this work included strong
790 VNIR absorbance bands characteristic of dioctahedral Al and Fe smectites; changes in clay mineralogy
791 with depth, primarily observed in the 2.1-2.5 micron range; illuvial accumulation of clay minerals into
792 subsurface (Bt) horizons; destruction of sedimentary bedding in weathered upper layers (A and B
793 horizons); preservation of relict bedding in unweathered bottom layers (C horizons); and centimeter-scale
794 changes in color and composition. These are all diagnostic features of terrestrial soils and should be
795 considered permissive evidence of pedogenic alteration on Mars. Spectral features of diagenetic
796 alterations included absorbances characteristic of zeolites and hematite. On Mars, these may indicate
797 zeolitization and burial dehydration of iron (oxy)hydroxides, respectively. These and other forms of
798 diagenesis are common in terrestrial paleosols that formed from weathering of volcaniclastic sediments [18]
799 and may also explain occurrences of zeolites [92] and hematite [51] detected from orbit in putative weathering
800 sequences on Mars.
801   This study provides a protocol for constraining climate and habitability from the geochemistry of
802 weathering profiles on Mars. Molecular weathering ratios that have been well studied in terrestrial
803 paleosols (e.g.,[31,93]) could be useful for interpreting climate and habitability of weathering profiles on
804 Mars. By using a suite of molecular weathering ratios and geochemical climofunctions (Figure 4), a
805 reconstruction of the climate and nature of weathering can be inferred from weathering profiles on Mars.
806 However, differences in the nature of weathering and diagenesis between Earth and Mars present
807 challenges for making direct comparisons. Such differences include a presumably anoxic early Mars
808 atmosphere that perhaps led to Fe^{2+} mobility during subaerial weathering [24], and the apparent absence of
809 plate tectonics which has implications for the nature and severity of diagenesis of weathering profiles on
810 Mars [3,94]. One additional consideration is application of the chemical index of alteration to weathering
811 profiles on Mars that were subject to weathering by acidic and sulfur-rich fluids. Weathering indices such
812 as CIA may not accurately reflect acid sulfate weathering of mafic Fe/Mg rich sediments because
813 weathering rates of mafic materials such as olivine proceeds more efficiently than feldspars, especially
814 under acidic conditions [95]. In addition, acidic conditions also affect the mobility of alkaline elements
815 which may further confuse interpretations of weathering intensity by examining CIA [51]. Martian
816 weathering profiles that were altered by fluids with circumneutral pH are better candidates for
817 application of molecular weathering ratios, weathering indices, and geochemical climofunctions
818 commonly applied to terrestrial paleosols.
819   The mineralogy and diagenetic alteration of paleosols also has implications for biosignature
820 preservation in Martian weathering profiles. Biosignatures in paleosols can include biomarkers,
821 biominerals, macro and microstructures and textures, chemistry, and isotopes [26], and the rapid burial that
822 characteristically entombs paleosols often creates favorable taphonomic environments for the preservation
823 of biosignatures. However, the preservation of chemical and isotopic biosignatures often relies on the
824 bulk abundance of organic matter preserved in a sample. Many factors contribute to the preservation and
825 degradation of organic matter in terrestrial paleosols including redox state prior to burial, clay
826 mineralogy, amorphous phase compositions and abundance, diagenetic alterations, and interactions with
827 sulfur (e.g., sulfurization) [15,43]. Redox state provides a first-order control on the preservation of organic

828   carbon in rapidly buried soils [43]; for example, soils forming under reducing conditions (e.g., wetlands)
829   generally preserve higher abundances of organics relative to those forming in oxidized, well-drained
830   conditions. Oxidized and Al-smectite rich paleosols such as those examined here are associated with
831   longer organic carbon residence time relative to kaolin group clays [96], but well-drained, oxidizing
832   conditions before burial are associated with severe losses of organic C after burial [18,43]. In addition, most
833   types of diagenetic alterations commonly observed in terrestrial paleosols are associated with the
834   degradation of organic matter. Illitization, zeolitization and celadonization may facilitate desorption of
835   organic carbon held on mineral surfaces, interlayer spaces, and crystal edges, thus possibly contributing to
836   burial-induced degradation of organic matter [97,98], though several authors have reported that early
837   diagenetic smectite-illite transformation may be facilitated by microbes [98–100] which has implications for
838   biosignature preservation in illite-rich soils. In this work, illitization and celadonization of smectite was
839   not observed, but zeolitization of amorphous colloids and/or poorly crystalline smectite may have
840   liberated adsorbed or chemisorbed organic carbon [101] and likely contributed to the degradation of the bulk
841   organic fraction. One the other hand, diagenetic features of paleosols such as burial gleization observed in
842   this work (Table S1 and Figure 3) may indicate organic carbon enrichment and the preservation of
843   chemical biosignatures in the surface horizons of paleosols. The drab green surface layer of the uppermost
844   paleosol examined in this work showed an accumulation of Fe^{2+} attributed to diagenetic burial gleization
845   via anaerobic microbial decay of organic matter. Previous investigations showed that this gleyed layer
846   was enriched in organic carbon relative to deeper layers in the paleosol [43], and thus burial gleization
847   features most likely constitute a chemical biosignature in paleosols. If features resembling burial
848   gleization are detected in upper layers of weathering profiles on Mars, they should be considered a high-
849   priority location for *in-situ* biosignature investigation.

850
851   **Conclusions**
852   The objective of this study was to analyze the mineralogy and diagenetic alterations of paleosols
853   from eastern Oregon, USA using techniques similar to those utilized by current and future missions to
854   Mars. Samples were gathered from three successive paleosol profiles in the early Oligocene (33 Ma)
855   middle Big Basin Member of the John Day Formation that formed from pedogenic weathering of volcanic
856   ash and tuff. Visible/near infrared spectroscopy, X-ray diffraction and evolved gas analysis confirmed
857   dioctahedral smectite was the major phase in all samples, with most samples primarily containing a
858   mixture of montmorillonite (Al smectite) and nontronite (Fe smectite). Minor phases detected with x-ray
859   diffraction included Opal-CT, cristobalite, andesine and gypsum. All samples contained minor amounts of
860   the zeolite mineral clinoptilolite which most likely formed from the diagenetic Ostwald ripening of
861   amorphous or nanocrystalline phases such as allophane, imogolite and/ or poorly crystalline smectite.
862   Across all samples only minor (< 5 wt. %) abundances of amorphous phases were observed; instead, most
863   samples contained between 70-95 wt. % crystalline clay minerals.
864   The mineralogy and morphology of paleosols examined here is consistent with formation under
865   well-drained, oxidizing conditions with moderate weathering rates. Geochemical climofunctions based on
866   molecular weathering ratios applied to these paleosols indicate soil formation under mean annual
867   precipitation of ~600 mm and mean annual temperature of approximately 10° C. Pedogenic weathering of
868   volcanic ash under these climatic conditions was sufficient to transform volcanic glass and
869   amorphous/nanocrystalline phases into strongly crystalline dioctahedral clay minerals.
870   Four types of alteration after burial that have affected paleosols examined in this work are 1)
871   Drab green surface horizons due to burial gleization of organic matter; 2) brick-red color from burial-
872   induced dehydration of ferric oxides and hydroxides; 3) zeolitization of volcanic glass and/or poorly
873   crystalline phases; and 4) significant mechanical compaction. Burial gleization, limited to the surface
874   horizons of paleosols, was most likely an early diagenetic alteration that resulted from the chemical
875   reduction of iron hydroxides and oxides by anaerobic bacteria consuming buried organic matter at or
876   below the water table. The timing of burial dehydration of (oxy)hydroxides remains poorly constrained,
877   but late diagenetic alterations such as zeolitization may have occurred during early Miocene burial at

878 depths of 380 to 1200 meters and temperatures of 27-55° C during deposition of the overlying Mascall
879 and Rattlesnake Formations. The current overburden of ~2 km has also resulted in the mechanical
880 compaction of paleosol profiles to approximately 70% of their original thickness before burial. Despite
881 significant overburden, absence of illite/chlorite and celadonite imply a lack of diagenetic K-metasomism
882 and celadonization, respectively. The high clay mineral content (up to 95 wt. %) of paleosols from the
883 middle Big Basin Member of the John Day Formation may have insulated profiles from diagenetic
884 alterations which have pervasively altered stratigraphically higher and less clay mineral-rich (~40 wt. %)
885 paleosols in the overlying Turtle Cove member of the John Day Formation.
886   On Mars, there are distinct stratigraphic changes in clay mineral and amorphous phase abundance
887 in sedimentary rocks across the Mawrth Vallis region and these general stratigraphic trends are observed
888 in the eastern Oregon paleosol sequence. Mineralogical changes across the compositional stratigraphy at
889 Muara Crater, Mawrth Vallis are comparable to the up-section decline in crystalline clay minerals and
890 subsequent increase in Al smectite, amorphous phases and hydrated silica through the Clarno and John
891 Day Formations resulting from the aridification of eastern Oregon during the late Eocene and Oligocene.
892 Strong spectral signatures of a nanophase aluminosilicate consistent with allophane and /or imogolite
893 have been noted at the stratigraphically highest layers across the Mawrth Vallis region and are thought to
894 represent a cool and dry climate where nanophase aluminosilicates resulted from minor alteration of
895 volcanic ash [40], and these uppermost layers share mineralogical similarities with the Turtle Cove Member
896 paleosols. In contrast, the lowermost layers at Mawrth Vallis have strong spectral signatures of crystalline
897 Fe/Mg smectite and are perhaps more akin to deeply weathered paleosols from the Clarno and lower John
898 Day Formations.
899   Pedogenic features observed in this work include dioctahedral smectite mineralogy, a clay
900 mineral doublet feature observed with VNIR spectroscopy possibly resulting from isomorphous
901 substitutions during pedogenic weathering, destruction of sedimentary bedding, sub-meter scale
902 differences in composition and color, and illuvial accumulation of clay minerals into subsurface horizons,
903 all of which resulted from precipitation-driven pedogenic weathering of andesitic to rhyodacitic volcanic
904 ash and tuff. Results from this work can help distinguish paleosols and weathering profiles from other
905 types of sedimentary rocks in the geological record of Mars.
906

907 Additional Information

908 Acknowledgements

918
919

920 Author Contribution Statement

921 A.P.B designed the study, performed laboratory analyses and drafted the manuscript. B.H.H identified
922 similarities between Mars and John Day paleosols, assisted with fieldwork and provided VNIR spectra of
923 paleosols. J.V.C guided all thermal analyses and facilitated data interpretation. B.S, J.V.C and D.W.M
924 contributed to data analysis and interpretation. V.T. performed x-ray diffraction and assisted with
925 interpretation of mineralogy. L.C.R.S aided with comparisons of modern soils with paleosols and
926 supervised the project. All authors contributed to the manuscript.
927

928 Author Disclosure Statement

929 No competing financial interests exist.

930 **Supplementary data is available online at:**
931
932
933

934 1. Bishop, J. . et al. Phyllosilicate Diversity and Past Aqueous Activity Revealed at Mawrth Vallis,
935 Mars. *Science* 830–834 (2008).

936 2. Bishop, J. L. *et al.* What the ancient phyllosilicates at Mawrth Vallis can tell us about possible
937 habitability on early Mars. *Planet. Space Sci.* **86**, 130–149 (2013).

938 3. Scheller, E. L., Ehlmann, B. L., Hu, R., Adams, D. J. & Yung, Y. L. Long-term drying of Mars by
939 sequestration of ocean-scale volumes of water in the crust. *Science (80-.).* **372**, 56–62 (2021).

940 4. Ye, B. & Michalski, J. R. Precipitation-Driven Pedogenic Weathering of Volcaniclastics on Early
941 Mars. *Geophys. Res. Lett.* **48**, 1–10 (2021).

942 5. Murchie, S. *et al.* Compact Reconnaissance Imaging Spectrometer for Mars (CRISM) on Mars
943 Reconnaissance Orbiter (MRO). *J. Geophys. Res.* **112**, 1–57 (2007).

944 6. Carter, J., Loizeau, D., Mangold, N., Poulet, F. & Bibring, J. Widespread surface weathering on
945 early Mars : A case for a warmer and wetter climate. *Icarus* **248**, 373–382 (2015).

946 7. Loizeau, D. *et al.* Quantifying widespread aqueous surface weathering on Mars : The plateaus
947 south of Coprates Chasma. *Icarus* **302**, 451–469 (2018).

948 8. Franklin, R. *et al.* Oxia Planum : The Landing Site for the ExoMars. *Astrobiology* **21**, 1–22 (2021).

949 9. Bristow, T. F. *et al.* Clay mineral diversity and abundance in sedimentary rocks of Gale crater ,
950 Mars. *Sci. Adv.* **4**, 1–9 (2018).

951 10. Ehlmann, B. L., Mustard, J. F. & Murchie, S. L. Geologic setting of serpentine deposits on Mars.
952 *Geophys. Res. Lett.* **37**, 1–5 (2010).

953 11. Ehlmann, B. L. *et al.* Clay minerals in delta deposits and organic preservation potential on Mars.
954 *Nature* **1**, 355–358 (2008).

955 12. Michalski, J. R. *et al.* Constraints on the crystal-chemistry of Fe / Mg-rich smectitic clays on Mars
956 and links to global alteration trends. *Earth Planet. Sci. Lett.* **427**, 215–225 (2015).

957 13. Vaniman, D. T. *et al.* Mineralogy of a Mudstone at Yellowknife Bay , Gale Crater , Mars
958 Mineralogical Analysis and Quantitative Mineralogy. *Science (80-.).* 1–14 (2014)
959 doi:10.1126/science.1243480.

960 14. Bishop, J. L. *et al.* Surface clay formation during short-term warmer and wetter conditions on a
961 largely cold ancient Mars. *Nat. Astron.* **2**, 206–213 (2018).

962 15. Horgan, B., Bishop, L., Christensen, P. R. & Bell, J. F. Potential ancient soils preserved at Mawrth
963 Vallis from comparisons with Eastern Oregon paleosols: Implications for Early Martian Climate.
964 *Third Conf. Early Mars* **7074**, 12–13 (2012).

965 16. Cannon, K. M., Stephen, W. & Mustard, J. . Primordial clays on Mars formed beneath a steam or
966 supercritical atmosphere. *Nature* **552**, 88–91 (2017).

967 17. Ehlmann, B. L. *et al.* Subsurface water and clay mineral formation during the early history of
968 Mars. *Nature* **479**, 53–60 (2011).

969 18. Retallack, G. J. *Soil of the Past*. (Wiley Blackwell, 2019).

970 19. Smith, R. . & Horgan, B. H. N. Nanoscale Variations in Natural Amorphous and Nanocrystalline

971   Weathering Products in Mafic to Intermediate Volcanic Terrains on Earth : Implications for
972   Amorphous Detections on Mars. *J. Geophys. Res. Planets* **126**, 1–30 (2021).

973   20.   Horgan, B. Strategies for Searching for Biosignatures in Ancient Martian Sub-Aerial Surface
974   Environments. *Biosignature Preserv. Detect. Mars Analog Environ.* 7463 (2016)
975   doi:10.1089/ast.2016.1627.

976   21.   Rye, R. & Holland, H. Life associated with a 2 . 76 Ga ephemeral pond ?: Evidence from Mount
977   Roe # 2 paleosol. *Geology* **28**, 483–486 (2000).

978   22.   Heard, A. W. *et al.* Anoxic continental surface weathering recorded by the 2.95 Ga Denny Dalton
979   Paleosol (Pongola Supergroup, South Africa). *Geochim. Cosmochim. Acta* **295**, 1–23 (2021).

980   23.   Heard, A. W. & Kite, E. S. A probabilistic case for a large missing carbon sink on Mars after 3.5
981   billion years ago. *Earth Planet. Sci. Lett.* **531**, 116001 (2020).

982   24.   Liu, J. *et al.* Anoxic chemical weathering under a reducing greenhouse on early Mars. *Nat. as*
983   (2021) doi:https://doi.org/10.1038/s41550-021-01303-5.

984   25.   Retallack, G. J. Paleosols and paleoenvironments of early Mars. *Geology* **42**, 755–758 (2014).

985   26.   Hays, L. E. *et al.* Biosignature Preservation and Detection in Mars Analog Environments.
986   *Astrobiology* **17**, 363–400 (2017).

987   27.   Lantz, C. *et al.* Planetary Terrestrial Analogues Library project: 1. characterization of samples by
988   near-infrared point spectrometer. *Planet. Space Sci.* **189**, 104989 (2020).

989   28.   Bestland, E. . Alluvial Terraces and Paleosols As Indicators Of Early Oligocene Climate Change
990   (John-Day Formation, Oregon). *J. Sediment. Res.* **67**, 840–855 (1997).

991   29.   Retallack, G. J., Bestland, E. . & Fremd, T. . Eocene and Oligocene Paleosols of Central Oregon.
992   *Geol. Soc. Am. Spec. Pap.* **344**, 1–192 (2000).

993   30.   Smith, R. ., Horgan, B., Rampe, E. & Dehouck, E. The Composition of Amorphous Phases in
994   Soils and Sediments on Earth and Mars. *49th Lunar Planet. Sci. Conf. 2018* 14–15 (2018).

995   31.   Sheldon, N. D., Retallack, G. J. & Tanaka, S. Geochemical Climofunctions from North American
996   Soils and Application to Paleosols across the Eocene - Oligocene Boundary in Oregon
997   Geochemical Climofunctions from North American Soils and Application to Paleosols across the
998   Eocene-Oligocene Boundary in Or. *J. Geol.* **110**, 687–696 (2015).

999   32.   Staff, S. S. Keys to Soil Taxonomy. *United States Dep. Agric.* **12**, (2014).

1000   33.   Bestland, E. A. Fossil Andisols identified with mass-balance geochemistry (Oligocene John Day
1001   Formation, Oregon, U.S.A.). *J. Sediment. Res.* **72**, 673–686 (2002).

1002   34.   Milliken, R. ., Mustard, J. ., Ehlmann, B. L., Bishop, J. L. & Murchie, S. L. Interpreting and
1003   constraining the compositional and depositional environments of phyllosilicates on Mars. *Gr.*
1004   *Truth From Mars* **4036**, 7–8 (2008).

1005   35.   Bishop, J. L. *et al.* Multiple mineral horizons in layered outcrops at Mawrth Vallis, Mars, signify
1006   changing geochemical environments on early Mars. *Icarus* **341**, 113634 (2020).

1007   36.   Deit, L. Le *et al.* Extensive surface pedogenic alteration of the Martian Noachian crust suggested
1008   by plateau phyllosilicates around Valles Marineris. *J. Geophys. Res.* **117**, 1–25 (2012).

1009   37.   Dobrea, E. Z. N. *et al.* Mineralogy and stratigraphy of phyllosilicate - bearing and dark mantling
1010   units in the greater Mawrth Vallis / west Arabia Terra area : Constraints on geological origin. *J.*
1011   *Geophys. Res.* **115**, 1–27 (2010).

1012   38.   Lowe, D. R. *et al.* Deposition of > 3 . 7 Ga clay-rich strata of the Mawrth Vallis Group, Mars, in
1013   lacustrine, alluvial, and aeolian environments. *GSA Bull.* 17–30 (2020).

1014 39. Loizeau, D. *et al.* History of the clay-rich unit at Mawrth Vallis, Mars: High- resolution mapping
1015   of a candidate landing site. *J. Geophys. Res. Planets* 1820–1846 (2015)
1016   doi:10.1002/2015JE004894.Received.

1017 40. Bishop, J. . *et al.* Mineralogy of layered outcrops at Mawrth Vallis and implications for early
1018   aqueous geochemistry on Mars. *47th Lunar Planet. Sci. Conf.* **2**, 2–3 (2016).

1019 41. Retallack, G. J. Palaeosols of the Siwalik Group as a 15 Myr record of South Asian palaeoclimate.
1020   *Mem. - Geol. Soc. India* **32**, 36–51 (1995).

1021 42. Horgan, B. H. N. CLIMATE CHANGE AND A SEQUENCE OF HABITABLE ANCIENT
1022   SURFACE ENVIRONMENTS PRESERVED IN PEDOGENICALLY ALTERED SEDIMENTS
1023   AT MAWRTH VALLIS, MARS. in *Lunar and Planetary Science Conference* 3059 (2013).

1024 43. Broz, A. P. Organic Matter Preservation in Ancient Soils of Earth and Mars. *Life* **10**, (2020).

1025 44. Butt, C. R. M., Lintern, M. J. & Anand, R. R. Evolution of regoliths and landscapes in deeply
1026   weathered terrain — implications for geochemical exploration. *Ore Geol. Rev.* **16**, 167–183
1027   (2000).

1028 45. Zauyah, S., Schaefer, C. E. G. R. & Simas, F. N. B. *Saprolites. Interpretation of*
1029   *Micromorphological Features of Soils and Regoliths* (Elsevier B.V., 2018). doi:10.1016/b978-0-
1030   444-63522-8.00003-6.

1031 46. Beukes, N. J., Dorland, H., Nedachi, M. & Ohmoto, H. Tropical laterites, life on land and the
1032   history of atmospheric oxygen in the Paleoproterozoic. *Geology* **30**, 491–494 (2002).

1033 47. Rye, R., Geological, D. & Sciences, P. Life associated with a 2 . 76 Ga ephemeral pond ?:
1034   Evidence from Mount Roe # 2 paleosol. *Geology* 483–486 (2000).

1035 48. Watanabe, Y., Martin, J. E. . & Ohmoto, H. Geochemical evidence for terrestrial ecosystems 2.6
1036   billion years ago. *Nature* **408**, (2000).

1037 49. Watanabe, Y., Stewart, B. W. & Ohmoto, H. Organic- and carbonate-rich soil formation ~2.6
1038   billion years ago at Schagen, East Transvaal district, South Africa. *Geochim. Cosmochim. Acta* **68**,
1039   2129–2151 (2004).

1040 50. Horgan, B., Baker, L., Carter, J. & Chadwick, O. Where is the climate signature in the mineral
1041   record of early Mars? *Fourth Conf. Early Mars 2017* **3077**, 2014–2015 (2017).

1042 51. Liu, J., Michalski, J. R. & Zhou, M. Intense subaerial weathering of eolian sediments in Gale
1043   crater, Mars. *Sci. Adv.* **7**, (2021).

1044 52. Barrington, M. . *et al.* Mastcam-Z Analog Spectral Imager. *51st Lunar Planet. Sci. Conf.* **1595**,
1045   51–52 (2020).

1046 53. Horgan, B. *et al.* New constraints from CRISM and MASTCAM spectra on the mineralogy and
1047   origin of Mt. Sharp geologic units, Gale Crater, Mars. *48th Lunar Planet. Sci. Conf.* **3021**, 2–3
1048   (2017).

1049 54. Rampe, E. B. *et al.* Mineralogy and geochemistry of sedimentary rocks and eolian sediments in
1050   Gale crater, Mars: A review after six Earth years of exploration with Curiosity. *Geochemistry* **80**,
1051   (2020).

1052 55. Morris, R. V. *et al.* Silicic volcanism on Mars evidenced by tridymite in high-SiO2 sedimentary
1053   rock at Gale crater. *Proc. Natl. Acad. Sci. U. S. A.* **113**, 7071–7076 (2016).

1054 56. Mahaffy, P. R. *et al.* The sample analysis at mars investigation and instrument suite. *Space Sci.*
1055   *Rev.* **170**, 401–478 (2012).

1056 57. Goesmann, F. *et al.* The Mars Organic Molecule Analyzer (MOMA) Instrument: Characterization
1057   of Organic Material in Martian Sediments. *Astrobiology* **17**, 655–685 (2017).

1058 58. Bishop, J. L., Lane, M. D., Dyar, M. D. & Brown, A. J. Reflectance and emission spectroscopy
1059   study of four groups of phyllosilicates: smectites, kaolinite-serpentines, chlorites and micas. *Clay*
1060   *Miner.* **43**, 35–54 (2008).

1061 59. Jones, R. C., Babcock, C. J. & Knowlton, W. B. Estimation of the Total Amorphous Content of
1062   Hawai'i Soils by the Rietveld Method. *Soil Sci. Soc. Am. J.* **1108**, 1100–1108 (2000).

1063 60. Chipera, S. J. & Bish, D. L. Baseline studies of the clay minerals society source clays: Colloid and
1064   surface phenomena. *Clays Clay Miner.* **49**, 446–452 (2001).

1065 61. Breecker, D. O., Sharp, Z. D. & McFadden, L. D. Seasonal bias in the formation and stable
1066   isotopic composition of pedogenic carbonate in modern soils from central New Mexico, USA.
1067   *Bull. Geol. Soc. Am.* **121**, 630–640 (2009).

1068 62. Retallack, G. J. *et al.* Late Pleistocene mammoth trackway from Fossil Lake , Oregon.
1069   *Paleogeography, Paleoclimatology, Paleoecol.* (2018) doi:10.1016/j.palaeo.2018.01.037.

1070 63. Lukens, W. E., Nordt, L. C., Stinchcomb, G. E., Driese, S. G. & Tubbs, J. D. Reconstructing pH of
1071   paleosols using geochemical proxies. *J. Geol.* **126**, 427–449 (2018).

1072 64. Chemtob, S. M., Nickerson, R. D., Morris, R. V., Agresti, D. G. & Catalano, J. G. Synthesis and
1073   structural characterization of ferrous trioctahedral smectites: Implications for clay mineral genesis
1074   and detectability on Mars. *J. Geophys. Res. E Planets* **120**, 1119–1140 (2015).

1075 65. Yant, M. *et al.* Visible , near-infrared , and mid-infrared spectral characterization of Hawaiian
1076   fumarolic alteration near Kilauea' s December 1974 flow: Implications for spectral discrimination
1077   of alteration environments on Mars. *Am. Mineral.* **103**, (2018).

1078 66. Danielson, J. . *et al.* Characterization of outcrops containing 'doublet' spectra at Mawrth Vallis,
1079   Mars. *Lunar Planet. Sci. Conf.* **2019**, 1–179 (2019).

1080 67. Horgan, B., Christensen, P. & Iii, J. F. B. Searching for pedogenic phyllosilicates in ancient
1081   martian soils. *AGU Fall Meet.* 1999 (2011).

1082 68. Horgan, B. *et al.* The effects of climate , environment , and diagenesis on the spectral properties of
1083   volcanic soils. in *GSA Annual Meeting, Cordilleran Section* 1–24 (2017).

1084 69. Novoselov, A. A., Roberto, C. & Filho, D. S. Potassium metasomatism of Precambrian paleosols.
1085   *Precambrian Res.* **262**, 67–83 (2015).

1086 70. Earnest, C. M. Thermal analysis of selected illite and smectite clay minerals. Part II. Smectite clay
1087   minerals. in *Thermal Analysis in the Geosciences* (eds. Smykatz-Kloss, W. & Warne, S. S. J.)
1088   288–312 (Springer Berlin Heidelberg, 1991).

1089 71. Mcadam, A. ., Sutter, B., Archer, P. ., Franz, H. . & Eigenbrode, J. . The chemistry and mineralogy
1090   of the Glen Torridon clay-bearing unit from Mars Science Laboratory Sample Analysis at Mars.
1091   *51st Lunar Planet. Sci. Conf.* **2243**, 60–74 (2020).

1092 72. Smith, R. J., Rampe, E. B., Horgan, B. H. N. & Dehouck, E. Deriving Amorphous Component
1093   Abundance and Composition of Rocks and Sediments on Earth and Mars. *J. Geophys. Res.*
1094   *Planets* **123**, 2485–2505 (2018).

1095 73. Sutter, B. *et al.* Evolved gas analyses of sedimentary rocks and eolian sediment in Gale Crater,
1096   Mars: Results of the Curiosity rover's sample analysis at Mars instrument from Yellowknife Bay
1097   to the Namib Dune. *J. Geophys. Res. Planets* 2574–2609 (2017) doi:10.1002/2016JE005225.

1098 74. Sutter, B., Laurer, H. ., Golden, D. ., Ming, D. . & Boynton, W. . PHOENIX LANDER'S
1099   THERMAL EVOLVED GAS ANALYZER: DIFFERENTIAL SCANNING CALORIMETER
1100   AND MASS SPECTROMETER DATABASE DEVELOPMENT. in *35th Lunar and Planetary*
1101   *Science Conference* vol. 21 1–3 (2008).

1102 75. Ming, D. W. *et al.* Volatile and Organic Compositions of Sedimentary Rocks in Yellowknife Bay ,
1103   Gale Crater , Mars. *Sci. Express* 1–15 (2014) doi:10.1126/science.1245267.

1104 76. Hogancamp, J. V *et al.* Identification of phyllosilicates in mudstone samples using water releases
1105   detected by the Sample Analysis at Mars (SAM) instrument in Gale Crater, Mars. *Lunar Planet.*
1106   *Sci. XLVIII* 1620 (2017) doi:10.1126/science.1243480.

1107 77. Mcadam, A. . *et al.* Constraints on Gale Crater mudstone from MSL SAM evolved water. in *Lunar*
1108   *and Planetary Science XLVIII* 7–8 (2017). doi:10.1126/science.1245267.

1109 78. Mcadam, A. . *et al.* Sulfur-bearing phases detected by evolved gas analysis of the Rocknest
1110   aeolian deposit, Gale Crater, Mars. *J. Geophys. Res. Planets* **119**, 6121–6139 (2014).

1111 79. François, P. *et al.* Magnesium sulfate as a key mineral for the detection of organic molecules on
1112   Mars using pyrolysis. *J. Geophys. Res. – Planets* 61–74 (2015)
1113   doi:10.1002/2015JE004884.Received.

1114 80. Driese, S. G. & Ober, E. G. Paleopedologic and paleohydrologic records of precipitation
1115   seasonality from early Pennsylvanian 'Underclay' paleosols, U.S.A. *J. Sediment. Res.* **75**, 997–
1116   1010 (2005).

1117 81. Retallack, G. J. Untangling the effects of burial alteration and ancient soil formation. *Annu. Rev.*
1118   *Earth Planet. Sci.* 183–206 (1991).

1119 82. PiPujol, M. D. & Buurman, P. The distinction between ground-water gley and surface-water gley
1120   phenomena in Tertiary paleosols of the Ebro basin, NE Spain. *Palaeogeogr. Palaeoclimatol.*
1121   *Palaeoecol.* **110**, 103–113 (1994).

1122 83. Allen, J. R. L. Time scales of colour change in late Flandrian intertidal muddy sediments of the
1123   Severn Estuary. *Proc. Geol. Assoc.* **97**, 23–28 (1986).

1124 84. Spinola, D. N. *et al.* Diagenetic reddening of Early Eocene paleosols on King George Island,
1125   Antarctica. *Geoderma* **315**, 149–159 (2018).

1126 85. Sheldon, N. D. Pedogenesis and geochemical alteration of the Pacific Gorge subgroup Columbia
1127   River basalt, Oregon. *Bull. Geol. Soc. Am.* **115**, 1377–1387 (2003).

1128 86. Solleiro-Rebolledo, E. *et al.* Paleosols beneath a lava flow in the southern basin of Mexico: The
1129   effect of heat on the paleopedological record. *Catena* **137**, 622–634 (2016).

1130 87. Ming, D. W. & Mumpton, F. . Zeolites in Soils. in *Minerals in Soil Environments* vol. 18 873–911
1131   (1989).

1132 88. Hay, R. . Stratigraphy and zeolitic diagenesis of the John Day formation of Oregon. **42**, 199–252
1133   (1963).

1134 89. Steefel, C. I. & Van Cappellen, P. A new kinetic approach to modeling water-rock interaction: The
1135   role of nucleation, precursors, and Ostwald ripening. *Geochim. Cosmochim. Acta* **54**, 2657–2677
1136   (1990).

1137 90. Chadwick, O. A. & Chorover, J. The chemistry of pedogenic thresholds. *Geoderma* **100**, 321–353
1138   (2001).

1139 91. Sclater, J. G. & Christie, P. Continental Stretching: An explanation of the Post-Mid-Cretaceous
1140   subsidence of the Central North Sea Basin. *J. Geophys. Res.* **85**, 3711–3739 (1980).

1141 92. Bishop, J. L. & Rampe, E. B. Evidence for a changing Martian climate from the mineralogy at
1142   Mawrth Vallis. *Earth Planet. Sci. Lett.* **448**, 42–48 (2016).

1143 93. Liivamägi, S. *et al.* Paleosols on the Ediacaran basalts of the East European Craton: a unique
1144   record of paleoweathering with minimum diagenetic overprint. *Precambrian Res.* (2018)
1145   doi:10.1016/j.precamres.2018.07.020.

1146 94. Tosca, N. J. & Knoll, A. H. Juvenile chemical sediments and the long term persistence of water at
1147 the surface of Mars. *Earth Planet. Sci. Lett.* **286**, 379–386 (2009).

1148 95. Berger, J. A. *et al.* Zinc and germanium in the sedimentary rocks of Gale Crater on Mars indicate
1149 hydrothermal enrichment followed by diagenetic fractionation. *J. Geophys. Res. Planets* 1747–
1150 1772 (2017) doi:10.1002/2017JE005290.

1151 96. Wattel-Koekkoek, E., Buurman, P., Van der Plicht, J., Wattel, E. & van Breeman, N. Mean
1152 residence time of soil organic matter associated with kaolinite and smectite. *Eur. J. Soil Sci.* **54**,
1153 269–278 (2003).

1154 97. Li, Y., Cai, J., Song, M., Ji, J. & Bao, Y. Influence of organic matter on smectite illitization : A
1155 comparison between red and dark mudstones from the Dongying Depression , China. *Am. Mineral.*
1156 **101**, 134–145 (2016).

1157 98. Elliott, W. C. & Matisoff, G. Evaluation of kinetic models for the smectite to illite transformation.
1158 *Clays Clay Miner.* **44**, 77–87 (1996).

1159 99. Fang, Q. *et al.* Applied Clay Science New insights into microbial smectite illitization in the
1160 Permo-Triassic. *Appl. Clay Sci.* **140**, 96–111 (2017).

1161 100. Becker-Kerber, B. *et al.* The role of volcanic-derived clays in the preservation of Ediacaran biota
1162 from the Itajaí Basin (ca. 563 Ma, Brazil). *Sci. Rep.* **11**, 1–10 (2021).

1163 101. Kaiser, K. & Guggenberger, G. The role of DOM sorption to mineral surfaces in the preservation
1164 of organic matter in soils. *Org. Geochem.* **31**, 711–725 (2000).

1165
1166

1167
1168

1169

1170